LKB1 specifies neural crest cell fates through pyruvate-alanine cycling

Anca Radu, Sakina Torch, Florence Fauvelle, Karin Pernet-Gallay, Anthony Lucas, Renaud Blervaque, Véronique Delmas, Uwe Schlattner, Laurence Lafanechère, Pierre Hainaut, et al.

DEVELOPMENTAL BIOLOGY

LKB1 specifies neural crest cell fates through pyruvate-alanine cycling

Anca G. Radu[1]*, Sakina Torch[1]*, Florence Fauvelle[2,3], Karin Pernet-Gallay[2], Anthony Lucas[1], Renaud Blervaque[1], Véronique Delmas[4], Uwe Schlattner[5,6], Laurence Lafanechère[1], Pierre Hainaut[1], Nicolas Tricaud[7], Véronique Pingault[8], Nadège Bondurand[8], Nabeel Bardeesy[9,10,11], Lionel Larue[4], Chantal Thibert[1†‡], Marc Billaud[1,12†‡]

Metabolic processes underlying the development of the neural crest, an embryonic population of multipotent migratory cells, are poorly understood. Here, we report that conditional ablation of the *Lkb1* tumor suppressor kinase in mouse neural crest stem cells led to intestinal pseudo-obstruction and hind limb paralysis. This phenotype originated from a postnatal degeneration of the enteric nervous ganglia and from a defective differentiation of Schwann cells. Metabolomic profiling revealed that pyruvate-alanine conversion is enhanced in the absence of *Lkb1*. Mechanistically, inhibition of alanine transaminases restored glial differentiation in an mTOR-dependent manner, while increased alanine level directly inhibited the glial commitment of neural crest cells. Treatment with the metabolic modulator AICAR suppressed mTOR signaling and prevented Schwann cell and enteric defects of *Lkb1* mutant mice. These data uncover a link between pyruvate-alanine cycling and the specification of glial cell fate with potential implications in the understanding of the molecular pathogenesis of neural crest diseases.

INTRODUCTION

Neural crest cells (NCCs) are highly invasive stem cells that originate from the dorsolateral folds of the neural tube and delaminate from the neuroepithelium through an epithelial-mesenchymal transition (*1*). NCCs migrate along stereotypical paths and give rise to a broad array of derivatives including most of the craniofacial skeleton, neuroendocrine tissues, and pigment cells. Furthermore, the peripheral nervous system, comprising sensory neurons and Schwann cells of the parasympathetic and sympathetic nervous systems, as well as neurons and glial cells that constitute the enteric nervous system, arises from NCCs. Defects in human neural crest development are the cause of a constellation of disorders called neurocristopathies. The most common clinical phenotypes include craniofacial abnormalities, hearing loss, absence of pigmentation, cardiac defects, and enteric ganglia agenesis (*2*). Although the cascade of molecular events that specify neural crest territories, orchestrate NCC delamination, and guide their polarized migration throughout the embryo has been extensively explored, the contribution of metabolic regulation to NCC formation and differentiation has received less attention. In this regard, morphogenesis requires adjustment of the metabolism of embryonic cells to cope with alterations in nutrient availability and tissue oxygenation specific to their microenvironment (*3*). The mapping of the metabolic pathways that are activated in early stem cells has begun to shed light on the respective contribution of glycolysis versus oxidative phosphorylation in the maintenance of pluripotency and cell fate commitment (*4*). However, the role of metabolic remodeling in later developmental stages, including the formation of neural crest derivatives, remains poorly understood.

The tumor suppressor liver kinase B1 (*LKB1*; also named *STK11*) encodes a serine/threonine kinase that has been evolutionarily conserved from invertebrates to mammals (*5*, *6*). Germline mutations of *LKB1* are responsible for the Peutz-Jeghers syndrome, a dominantly inherited cancer disorder, and somatic mutations of this gene have been associated with various cancers including lung and cervical tumors (*7*). The binding of LKB1 to the pseudokinase STRAD (STRADα or STRADβ) and the scaffolding molecule MO25 allosterically controls LKB1 catalytic activity and promotes its nuclear export (*8*). LKB1 acts as a key regulator of energy metabolism through the activation of the AMP (adenosine 5′-monophosphate)–activated protein kinase (AMPK), a sensor that adapts energy supply to the nutrient demands of cells facing situations of metabolic stress (*9*). AMPK phosphorylates a large array of substrates to achieve metabolic adaptation. In particular, AMPK phosphorylates the acetyl CoA (coenzyme A) carboxylase (ACC) to inhibit fatty acid synthesis (*10*, *11*) as well as two regulators of mammalian target of rapamycin complex 1 (mTORC1), RAPTOR and TSC2, to inhibit the mTOR pathway (*12*, *13*). In addition to AMPK, LKB1 also phosphorylates 12 AMPK-related kinases that regulate cell polarization, axon branching of cortical neurons, and hepatic neoglucogenesis (*14*–*17*).

We recently showed that Lkb1 governs delamination, migration, differentiation, and survival of cephalic NCC, these complex morphogenetic processes being essential for vertebrate head formation (*18*). To further understand the contribution of Lkb1 to the establishment of neural crest lineages, we disrupted this gene in a subset of vagal and truncal mouse NCC using the *tyrosinase* Cre (Tyr::Cre) transgene.

[1]Institute for Advanced Biosciences, INSERM U1209, CNRS UMR5309, Université Grenoble Alpes, 38000 Grenoble, France. [2]Univ. Grenoble Alpes, INSERM, U1216, Grenoble Institute of Neurosciences GIN, 38000 Grenoble, France. [3]Univ. Grenoble Alpes, INSERM, US17, MRI facility IRMaGe, 38000 Grenoble, France. [4]Institut Curie, Normal and Pathological Development of Melanocytes, CNRS UMR3347; INSERM U1021; Equipe Labellisée–Ligue Nationale Contre le Cancer, Orsay, France. [5]Laboratory of Fundamental and Applied Bioenergetics, Univ Grenoble Alpes, 38185 Grenoble, France. [6]INSERM U1055, 38041 Grenoble France. [7]INSERM U1051, Institut des Neurosciences de Montpellier (INM), Université de Montpellier, Montpellier, France. [8]INSERM U1163, Institut Imagine, Paris, France. [9]Cancer Center, Massachusetts General Hospital, 185 Cambridge Street, Boston, MA 02114, USA. [10]Center for Regenerative Medicine, Massachusetts General Hospital, 185 Cambridge Street, Boston, MA 02114, USA. [11]Department of Medicine, Harvard Medical School, Boston, MA 02114, USA. [12]"Clinical and experimental model of lymphomagenesis" Univ Lyon, Université Claude Bernard Lyon1, INSERM 1052, CNRS 5286, Centre Léon Bérard, Centre de recherche en cancérologie de Lyon, Lyon France.
*These authors contributed equally to this work.
†Corresponding author. Email: marc.billaud@lyon.unicancer.fr (M.B.); chantal.thibert@univ-grenoble-alpes.fr (C.T.)
‡Co-senior authors.

We now report that ablation of *Lkb1* in these NCC subpopulations impairs the differentiation of melanocytes, enteric ganglion cells, and Schwann cells. Metabolomic analyses combined with functional studies reveal that Lkb1 regulates pyruvate to alanine conversion and that inhibition of alanine aminotransferase (ALAT) rescues glial differentiation of *Lkb1*-null NCC in an mTOR-dependent manner. Last, we show that treatment of *Lkb1*-deficient mice with the metabolic modulator 5-aminoimidazole-4-carboxamide riboside (AICA riboside or AICAR) normalizes mTOR signaling and prevents Schwann cell and enteric defects. Together, our results provide evidence that Lkb1 specifies glial fate of NCC through metabolic pathways controlling pyruvate-alanine transamination.

RESULTS

Lkb1 deletion results in a complex neural crest phenotype

To explore in vivo Lkb1 functions during lineage establishment from NCCs, *Lkb1* conditional mutant mice ($Lkb1^{F/F}$) (*19*) were interbred to the *Tyr::Cre* deleter (*20*–*22*) and the *R26R* reporter (*23*) strains (fig. S1, A and B). The *tyrosinase* promoter is active from embryonic day 10.5 (E10.5) in subsets of NCC, thereby allowing the targeting of migrating melanoblasts, NCC-derived cells of the enteric nervous system, and precursors of the Schwann cell lineage (fig. S1C) (*20*, *21*, *24*). A role of Lkb1 in Schwann cell myelination and axon maintenance has been previously reported (*25*–*27*). However, our mouse model allows us to explore the role of Lkb1 during earlier stages of the Schwann cell lineage.

Homozygous *Lkb1*-deficient mice ($Lkb1^{F/F}$;$Tyr::Cre^{+/tg}$ referred to here as cKO) were born at the expected Mendelian ratio (fig. S1D) but showed either an almost complete lack of coat color pigmentation or white spotting (Fig. 1A and fig. S1E). Most of the cKO mice failed to thrive and died within a few weeks after birth (Fig. 1B). cKO mice exhibited a reduced weight gain (Fig. 1C) and a distended abdomen (fig. S1F). Necropsy revealed an intestinal pseudo-obstruction with abnormal dilation of the small intestine and/or colon, atrophy of the cecum, and, at a more advanced stage, a reduction of the stomach accompanied by hypertrophy of the cecum (Fig. 1D). The mutant mice also displayed substantially reduced mobility due to progressive hind limb paralysis (fig. S1G). When lifted by their tail, 21-day-old (P21) cKO mice reflexively contracted their limbs, sometimes unilaterally but more often bilaterally, whereas control littermates extended their legs when challenged to the same test (Fig. 1E). Gait tests were also performed by footprint analysis at P21 (fig. S1H). The stride distance was significantly reduced in cKO mice, while the sway distance was unaffected, resulting in a shorter gait in the absence of *Lkb1*. At the macroscopic level, the sciatic nerves of cKO mice appeared thinner and more translucent than in control littermates and lacked the characteristic banded pattern of myelin (Fig. 1F).

Thus, conditional deletion of *Lkb1* in truncal and vagal NCC results in a complex phenotype consisting of coat depigmentation, intestinal pseudo-obstruction, and a peripheral neuropathy.

Lkb1 loss impairs melanocyte formation

Using β-galactosidase (β-Gal) expression as a reporter of Cre expression, we observed that some, but not all, hair follicles from the skin on the back of wild-type (WT) and cKO mice expressed the Cre recombinase at P21 (fig. S2A). β-Gal staining on skin sections demonstrated that Cre expression was targeted to melanocytes in the hair bulb and in the hair bulge (fig. S2B) and was associated with decreased Lkb1 expression (Fig. 2A). The loss of Lkb1 did not impair melanoblast migration at E15.5 (Fig. 2B) but led to a drastic reduction of melanin-producing melanocytes in the hair follicles, as visualized by immunostaining of the melanin biosynthesis enzyme dopachrome tautomerase (Fig. 2C) and hematoxylin and eosin staining (fig. S2C).

Lkb1 inactivation causes enteric nervous system degeneration

We next explored the pathophysiological defects that lead to the intestinal pseudo-obstruction. By immunohistochemistry, *Lkb1* expression was observed in myenteric and submucosal plexuses in both the intestine and colon of P6 and P21 mice (Fig. 2D and fig. S3, A and B). The anti-Lkb1 antibody identified enteric ganglia because the labeling colocalized with the neuron-specific βIII-tubulin Tuj1 marker (fig. S3C). As expected, little or no Lkb1 was detected in the ganglia of cKO mice. Confocal analysis of β-Gal expression as the Cre reporter together with neural-specific (HuC/D) and glial-specific [glial fibrillary acidic protein (GFAP)] markers revealed staining in both neural and glial enteric cells (fig. S3D). A similar *LKB1* expression pattern was observed in human intestine and colon specimens (fig. S3E). Together, these results indicate that *Lkb1* is expressed in human and mouse enteric cells and that *Lkb1* inactivation occurred in neural and glial enteric cells.

To determine whether the enteric nervous system was affected in cKO mice, whole-mount staining of enteric neurons with the neural marker Tuj1 was performed at E15.5 (fig. S3F) and at birth (Fig. 2E). No overt sign of alteration of the enteric nervous system network was observed at both stages. However, at P6, cKO animals exhibited a clear reduction of the numbers of neural (Tuj1)– and glial (GFAP)–positive ganglia in the distal intestine and colon. The remaining ganglia were smaller in size and displayed punctiform morphology (fig. S3G). To visualize the enteric network at P21, acetylcholine esterase (AChE) staining was used. Although the neuronal network was clearly visible in the WT intestine, the staining was strongly diminished in *Lkb1*-deficient mice (Fig. 2F), as illustrated by the reduced percentage of surface covered by the cholinergic network (fig. S3H). The tunica muscularis and enterocyte epithelium had normal morphology. However, reduced size of intestinal villi in the distal intestine, probably due to fecal accumulation in the digestive tract, was frequently observed (fig. S3I). β-Gal expression on whole-mount intestine at P21 stained the enteric network in WT animals, whereas the enteric nervous system of cKO animals showed a drastic decrease of labeling (fig. S3J). These results were confirmed by measuring ganglia surfaces in relation to the length of tunica muscularis (fig. S3K). We also showed that global neural (Tuj1) staining was decreased in the absence of Lkb1, especially in ganglia inactivated for *Lkb1* (Fig. 2G and fig. S3L). Similarly, glial cell number was reduced upon *Lkb1* loss, as visualized with GFAP staining on intestine and colon sections of P21 mice (fig. S3M). The most frequently hypoganglionic area was the distal intestine, while the proximal colon was not affected (fig. S3N). The number of enteric neurons per length of tunica muscularis was 2-fold lower in the distal intestine of cKO animals and 1.6-fold lower in the distal colon as compared to WT controls (Fig. 2H). No sign of apoptosis was detected in enteric ganglia of cKO animals, neither with the TUNEL (terminal deoxynucleotidyl transferase–mediated deoxyuridine triphosphate nick end labeling) assay at P21 nor with the cleaved caspase-3 immunostaining at P6 (fig. S3O). These results show that *Lkb1* deficiency is associated with a progressive postnatal degeneration, leading to an enteric hypoganglionosis.

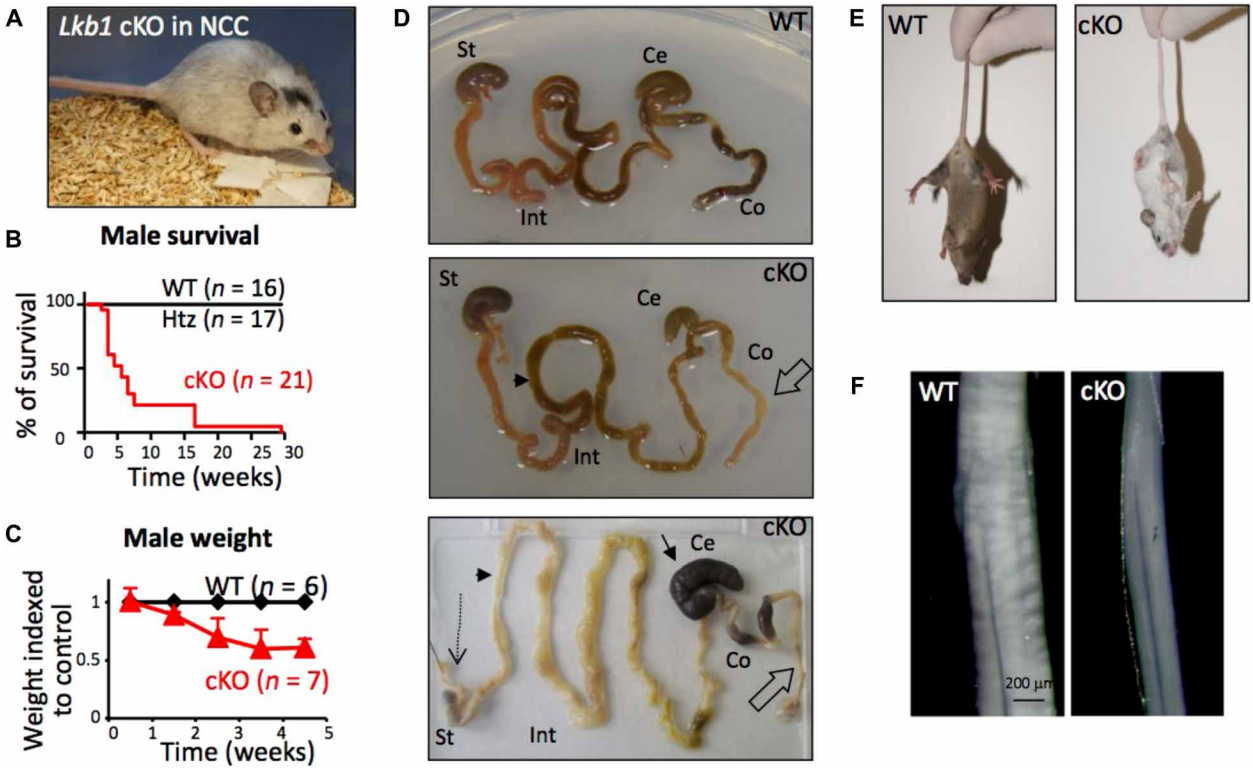

Fig. 1. Lkb1 loss leads to a complex neural crest phenotype. (**A**) Representative picture of a male animal with homozygous *Lkb1* ablation (*Lkb1* cKO) using the Tyr::Cre driver, which typically displays coat color hypopigmentation. (**B**) Kaplan-Meier graph comparing the survival of *Lkb1*-knockout (cKO), heterozygous (Htz), and WT male littermates. The number of animals is indicated above the curves. (**C**) *Lkb1* cKO mice rapidly lose weight compared to WT littermates (weight curves for cKO indexed to WT). (**D**) cKO mice develop a progressive intestinal pseudo-obstruction as shown at P21 (middle) by empty colon (Co) and atrophy of the cecum (Ce) and at adulthood (bottom) with atrophy of the stomach (St, dotted arrow), dilation of the small intestine (Int, arrow head), hypertrophy of the cecum (arrow), and colon constriction (empty arrow) compared to WT (top) ($n \geq 8$ mice per group). (**E**) Loss of hind limb extension reflex in *Lkb1 cKO* P21 mice compared to control animal (WT) manifested by hind limb clenching when lifted by the tail. (**F**) Appearance of sciatic nerves from control and *Lkb1* cKO mice at P21 showing myelinization defects in the mutant. Photo credits: Sakina Torch and Chantal Thibert, University Grenoble Alpes.

Lkb1 inactivation triggers a peripheral neuropathy

Lkb1 expression was detected on sciatic nerve sections at P6 and P21 (Fig. 2I and fig. S4A). A homogeneous staining of Lkb1 was observed in WT animals, while in cKO mice, Lkb1 staining was reduced. We next examined whether *Lkb1* was inactivated at embryonic stages in peripheral sensory axons, in glial cells, or in both by exploiting the *Tyr::Cre;Z/EG* mice (*28*). Labeling of neural crest–derived cells expressing the Cre recombinase, together with enhanced green fluorescent protein (EGFP), showed that glial GFAP-positive cells were also positive for EGFP (fig. S4B), whereas Tuj1-positive neurons were not positive for EGFP (fig. S4C). We also took advantage of the presence of the R26R reporter to stain semithin sections of sciatic nerves with X-Gal. These studies revealed labeling of Schwann cells but not of axons (fig. S4D). A sustained β-Gal activity was also detected in the dorsal root ganglia of either WT or cKO animals using Salmon Gal, another substrate of the β-Gal (fig. S4E). Immunofluorescence analyses of β-Gal expression in dorsal root ganglia demonstrated a clear colocalization with glial GFAP-positive cells but not with neuronal Tuj1-positive cells (fig. S4F). Together, these results indicate that *Lkb1* inactivation was restricted to glial cells and did not occur in sensory neurons.

We next examined the ultrastructure of sciatic nerves at P21 by transmission electron microscopy. Sciatic nerves of control animals were composed of myelinated sensory and motor axons of medium to large diameters and clusters of small-diameter unmyelinated sensory axons (Fig. 2J, a and b). Large clusters of unsorted axons were identified (Fig. 2J, c and d). Nonmyelinating Schwann cells of cKO mice did not enwrap axons individually as in WT animals but wrapped axons in bulk (Fig. 2J, b and d). Several axons achieved an appropriate 1:1 relationship with Schwann cells, but others showed aberrant sorting or remained unsorted (Fig. 2J, e and f). To quantify axon myelination defects in cKO animals, we measured the *g* ratio, the ratio of the axonal diameter to the myelinated fiber diameter. An increased *g* ratio was quantified in mutant mice (Fig. 2K), indicating hypomyelination of axons in cKO animals. The number of myelinated axons was reduced, and the degeneration of axons was also observed (fig. S4, G, and H). Along this line, neural Tuj1 staining was strongly reduced at both P6 and P21 (Fig. 2L and fig. S4I). As described previously (*26*, *27*), we also observed Schwann cell polarity defects using GFAP and E-cadherin staining (fig. S4, J and K). Together, these results yielded evidence that Lkb1 is required for the proper differentiation of Schwann cells.

Lkb1 controls glial fate specification

To explore the molecular mechanisms underlying these phenotypic defects, we first assessed the activation of AMPK by immunohistochemistry. Although total AMPK staining was not different between WT and

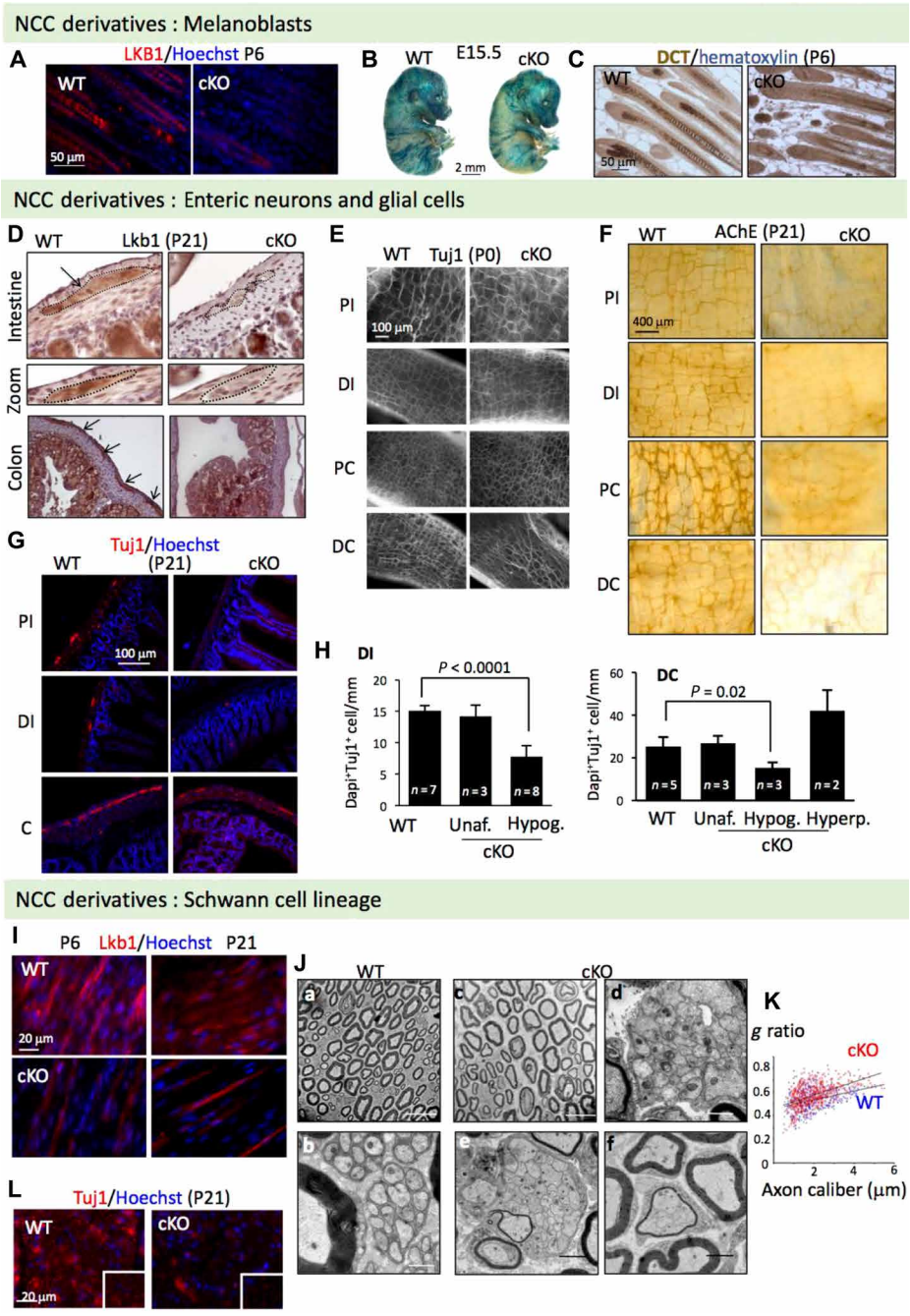

Fig. 2. Lkb1 is essential for the development of several neural crest derivatives. (**A**) Staining with Lkb1 antibody of back skin sections of P6 WT or Lkb1-inactivated (cKO). (**B**) Cre expression in migrating melanoblasts visualized by X-Gal staining of E15.5 embryos. (**C**) Staining for dopachrome tautomerase (DCT), one enzyme of melanin biosynthesis on skin sections. (**D**) Staining with Lkb1 D60C5 antibody (Cell Signaling) of myenteric ganglia in P21 mice in WT (arrows) and cKO animals. Ganglia are surrounded by dotted lines in the intestine and zooms are shown below. (**E**) Whole-mount Tuj1 labeling at birth (P0) on digestive tract from WT or *Lkb1* cKO animals [proximal (PI) and distal (DI) intestine; proximal (PC) and distal (DC) colon]. (**F**) Representative images of marked loss of enteric ganglia observed by whole-mount AChE staining of the enteric nervous system at P21. (**G**) Neural (Tuj1) staining on swiss-roll sections of the intestine and colon (WT, $n = 7$; cKO, $n = 12$). (**H**) Histograms indicating the average number of Dapi$^+$Tuj1$^+$ cells per millimeter of tunica muscularis in the distal intestine and distal colon. cKO animals with unaffected neuronal density (Unaf.), hypoganglionosis (Hypog.), or hyperplasia (Hyperp.) are plotted separately. Increased density of Tuj1-positive cells due to ganglia hyperplasia was observed in the distal colon of two of eight cKO analyzed. (**I**) Longitudinal sections of sciatic nerves of WT and *Lkb1* cKO mice at P6 (left) and P21 (right) immunostained with Lkb1 antibody. (**J**) Electron microscopy of sciatic nerves of P21 WT (a and b) and *Lkb1* cKO mice (c to f) showing myelinated nerve fibers (a and c) and unmyelinated axons in Remak bundles (b, d, and e). Sections of cKO nerves show aberrantly unsegregated axons of small to large diameter (d and e) and axonal sorting defects (e and f). Scale bars, 10 µm (a and c), 2 µm (e and f), and 1 µm (b and d). (**K**) Scatter plot of *g*-ratio values with linear regressions in sciatic nerves of WT (blue, $n = 400$ axons, 2 animals) and cKO (red, $n = 473$ axons, 3 animals). (**L**) Tuj1 immunostaining on transverse sections of P21 sciatic nerves. Insets show higher magnification of images with neural loss in cKO animals (WT, $n = 5$; cKO, $n = 3$).

cKO enteric ganglia (fig. S5A), AMPK phosphorylation at the LKB1 target residue, AMPKα^{Thr172}, was specifically decreased in the enteric ganglia of cKO mice, whereas no changes were seen in smooth muscle cell layers or enterocytes (Fig. 3A). In addition, an accumulation of Sox2-positive cells (Fig. 3B), which correspond to enteric progenitors and glial cells (*29*), was observed in the plexus ganglia of cKO mice, albeit no increase of glial cell number was detected (fig. S3M). We also observed an increase of enteric progenitors defined as cells expressing the low-affinity neurotrophin receptor p75^{NTR} (*30*, *31*) but not the neural marker Tuj1 (fig. S5B). Together, these data indicate that *Lkb1* deficiency is responsible for the lack of enteric progenitor differentiation.

Similarly, phospho-AMPK staining was markedly decreased in the absence of *Lkb1* on longitudinal sections of sciatic nerves (Fig. 3C), although there was no difference in total AMPK staining on sciatic nerves of WT and cKO animals (fig. S5C). While studying transverse and longitudinal sections of cKO sciatic nerves, an increased number of nuclei were observed at P6 and P21 (Fig. 3D). To assess the identity of these cells, we labeled immature/promyelinating Schwann cells with Sox2 (*32*). A net increase of Sox2-positive cells was observed in cKO mice at P6, and this was also evident, although at a lower extent at P21 (Fig. 3E). Similar results were obtained using p75^{NTR} as a marker of Schwann cell progenitors (*33*). In WT animals, p75^{NTR}-positive Schwann cells were mainly observed in association with axons and likely correspond to mature Schwann cells. In cKO animals, we quantified a threefold increase of p75^{NTR}-positive progenitor cells not associated with axons (fig. S5D). These data were also confirmed using an antibody that recognizes Krox20, a transcription factor that is a pivotal regulator of Schwann cell myelination (Fig. 3F). At P6, only a small fraction of Krox20-positive nuclei were detected in cKO animals, thus confirming that, in the absence of Lkb1, the differentiation of Schwann cell is delayed.

To examine the consequences of *Lkb1* inactivation on NCC fate at early stages of glial differentiation, we used the JoMa1.3 mouse neural crest stem cell line, which can be either maintained in a progenitor state or differentiated into glial cells (Fig. 3G) (*34*). Cells are kept in the progenitor state through the activation of the c-myc^{ER} oncoprotein, which exerts its transcription factor activity upon treatment of cells with 4-hydroxytamoxifen (4-OHT) (fig. S6A). In glial differentiation medium (without 4-OHT and supplemented with heregulin and forskolin), JoMa1.3 cells underwent morphological changes, acquiring a spindle shape (fig. S6, B and C). The induction of glial features was attested by staining for glial markers GFAP and S100 and by the loss of expression of the progenitor marker p75^{NTR} (Fig. 3H and fig. S6D). We validated the glial differentiation conditions with the glial marker GFAP, while no neural differentiation as assessed with the Tuj1 marker was observed (fig. S6E). We then established and validated a protocol to efficiently down-regulate *Lkb1* expression by transfecting *Lkb1* small interfering RNA (siRNA) either in progenitor cells or during NCC-derived glial differentiation (fig. S6F). *Lkb1* knockdown resulted in a reduction of AMPK phosphorylation (fig. S6, G to I). *Lkb1* loss led to a marked change of cell morphology during glial differentiation with the formation of dense network of actin stress fibers (fig. S6J). Expression of glial specific marker S100 or GFAP (Fig. 3I) was also reduced, and *p75^{NTR}* RNA expression was increased upon *Lkb1* knockdown (Fig. 3J). In addition, *Lkb1* loss did not trigger any neural differentiation (fig. S6K), thus confirming that these cells were maintained in a progenitor state. Collectively, our results provide evidence that Lkb1 is key to commit NCC-derived cells toward a glial cell fate.

Rewiring of metabolism in Lkb1-deficient nerves

To examine the metabolic changes induced upon *Lkb1* ablation in NCC derivatives, we investigated the metabolic status of sciatic nerves because they are the most NCC-enriched tissue compared to enteric nervous system and skin and it is the easiest structure to dissect out. We performed high-resolution magic angle spinning (HRMAS) proton nuclear magnetic resonance (NMR) spectroscopy, a technique that does not require previous solubilization of the samples. By applying this technique to structurally preserved nerves, the variations in both polar metabolite and lipid levels in *Lkb1* cKO sciatic were recorded (Fig. 4A). The broad resonances (L) arose from lipids and macromolecules, mainly methyl (L1) and methylene groups (L2 to L6) along fatty acid chains, while sharp peaks arose from small molecules, i.e., metabolites (Fig. 4, A and B). We could detect and assign 17 metabolites (fig. S7A), and the main spectral contributions were due to total creatine (*8*), phospholipid intermediates (*9*–*12*), taurine (*14*), and myo-inositol (*15*). Peaks corresponding to aliphatic chains of lipids and macromolecules were all down-regulated (fig. S7B). The multivariate statistical model showed a very good separation between the two mouse genotypes (fig. S7C), mainly due to the lower level of all acyl chain groups (L4 to L6).

These analyses also showed that the most striking changes in metabolite levels between WT and cKO groups could be ascribed to β-D-glucose (*17*), glutamate (*6*), and alanine (*2*). Quantification of these metabolites confirmed the statistically significant decrease in β-D-glucose and increase in alanine and glutamate levels in sciatic nerves of cKO animals (Fig. 4C). Together, these results indicate that *Lkb1* loss rewires the metabolism of a nervous tissue enriched in NCC derivatives (Fig. 4D).

Pyruvate-alanine transamination dictates glial differentiation

We used the JoMa1.3 cells to further explore the biological effects of alanine biosynthesis during glial cell commitment in vitro. Alanine concentration in JoMa1.3 cells cultured in glial differentiation medium was increased in the absence of *Lkb1* (Fig. 4E), thus validating the in vivo observations. In addition, we confirmed the accumulation of alanine in *Lkb1*-null mouse embryonic fibroblasts (MEFs; fig. S7D). Conversely, alanine was not increased in JoMa1.3 progenitor cells upon *Lkb1* knockdown (fig. S7E).

Lkb1 has been found to control the maturation of Schwann cells at later steps of Schwann cell differentiation by regulating citrate synthase activity (*26*). When citrate levels were measured in our model of early stage of glial commitment, no variation of this metabolite could be detected in the absence of *Lkb1*, neither in JoMa1.3 progenitors nor in glial cells (fig. S7F).

AMPK activation with its agonist 991 in WT MEF triggered a decrease of alanine concentration (Fig. 4F), whereas MEF cells doubly knocked out for AMPKα1/2 catalytic subunits exhibited a significant increased level of alanine (Fig. 4G). However, inhibition of salt-inducible kinases (SIK), which are activated by LKB1, with the compound HG-9-91-01 did not modify alanine levels in MEF (fig. S7, G and H). These data indicate that AMPK is a major effector downstream of LKB1 that contributes to the inhibition of alanine biosynthesis.

Our results support a mechanistic link between Lkb1 function and pyruvate-alanine transamination via the ALAT (Fig. 4H, left),

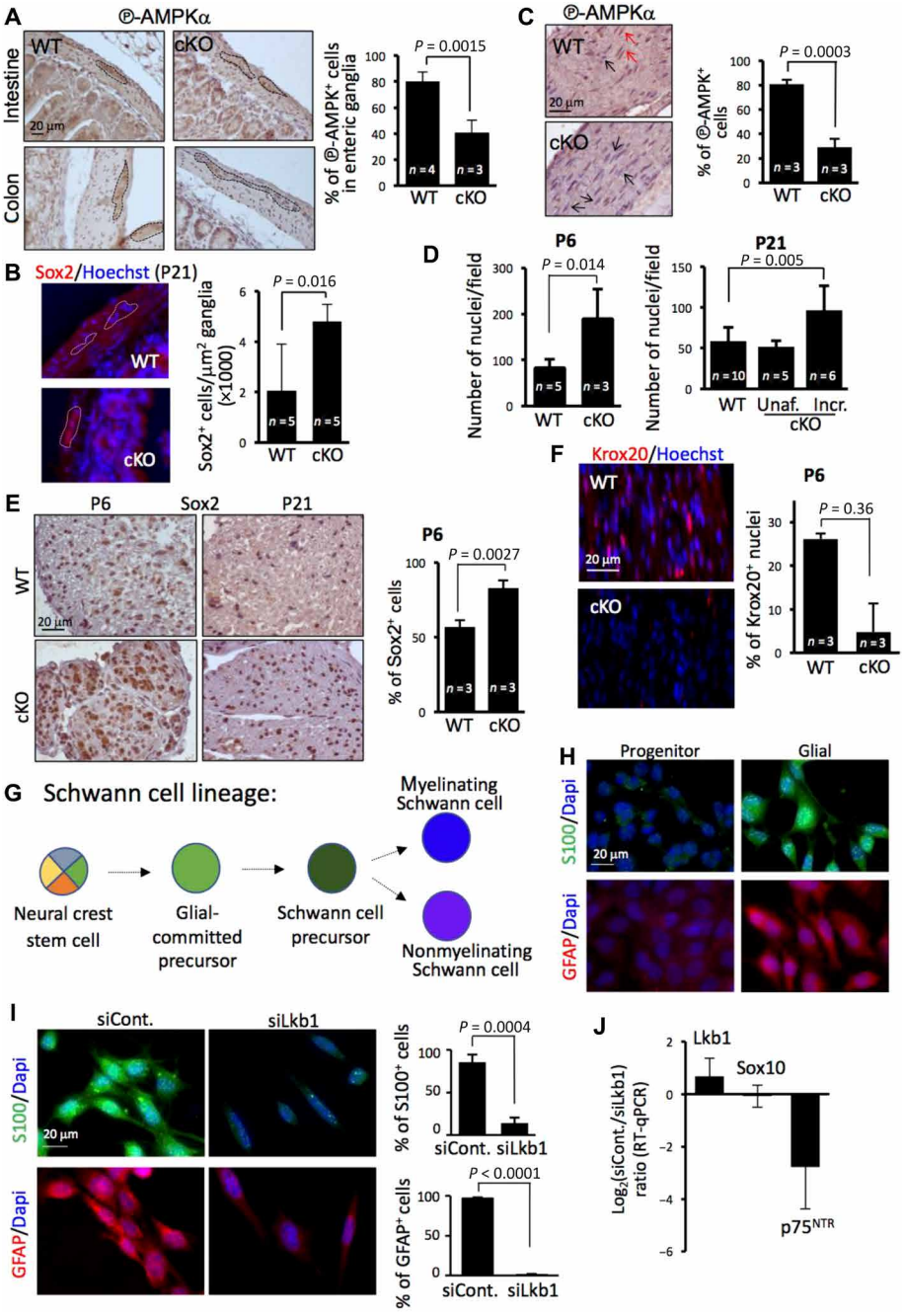

Fig. 3. Abnormal formation of NCC is associated with differentiation defects. (**A**) Immunohistochemistry for phospho-AMPKα1/2 in enteric nervous system of intestine and colon showing decreased phospho-AMPK staining in cKO animals. Myenteric ganglia are surrounded by dotted lines. Right: Quantification of positive cells in enteric ganglia. (**B**) Sox2 immunostaining to label progenitor/glial cells in the enteric nervous system on swiss-roll sections of distal intestine at P21. Right: Quantification of Sox2-positive cells per surface of myenteric ganglia. (**C**) Immunohistochemistry for phospho-AMPKα1/2 on longitudinal sections of sciatic nerves showing decreased phospho-AMPK staining in cKO animals. AMPK-positive cells are pointed out by red arrows, whereas black arrows designate AMPK-negative cells (blue nuclei). (**D**) Number of nuclei per field on transverse sections of sciatic nerves of P6 and P21 WT or *Lkb1* cKO mice. (**E**) Immunostaining for Sox2, a marker of Schwann cell precursors and immature Schwann cells, on nerve sections of WT and cKO animals. Right: Quantification at P6. (**F**) Krox20 immunostaining (red) to label myelinating Schwann cells at P6 in longitudinal sections of sciatic nerves. Right: Quantification at P6. (**G**) Schematic representation depicting first steps involved in glial commitment and later steps in Schwann cell from NCC. (**H**) Transformed mouse NCC JoMa1.3 cells were either maintained as progenitors or differentiated into glial cells (first steps of the lineage) as validated by staining against glial marker S100 (top panels, $n = 3$) or GFAP (bottom panels, $n = 3$). (**I**) Transfected JoMa1.3 cells during glial commitment with *Lkb1*-targeting siRNA (siLKB1) showed decrease of glial markers compared to nontargeting control siRNA (scramble, siCont.). GFAP, $n = 3$; S100, $n = 4$. Right: Percentages of positive cells. (**J**) Reverse transcription quantitative polymerase chain reaction (RT-qPCR) showing expression of *Sox10* and $p75^{NTR}$ genes in glial JoMa1.3 cells upon *Lkb1* silencing. Data are expressed as relative expression in control cells compared to siLkb1 cells (siCont./siLkb1, $n = 4$). Expression level of endogenous mouse *Lkb1* in JoMa1.3 cells is also shown ($n = 4$).

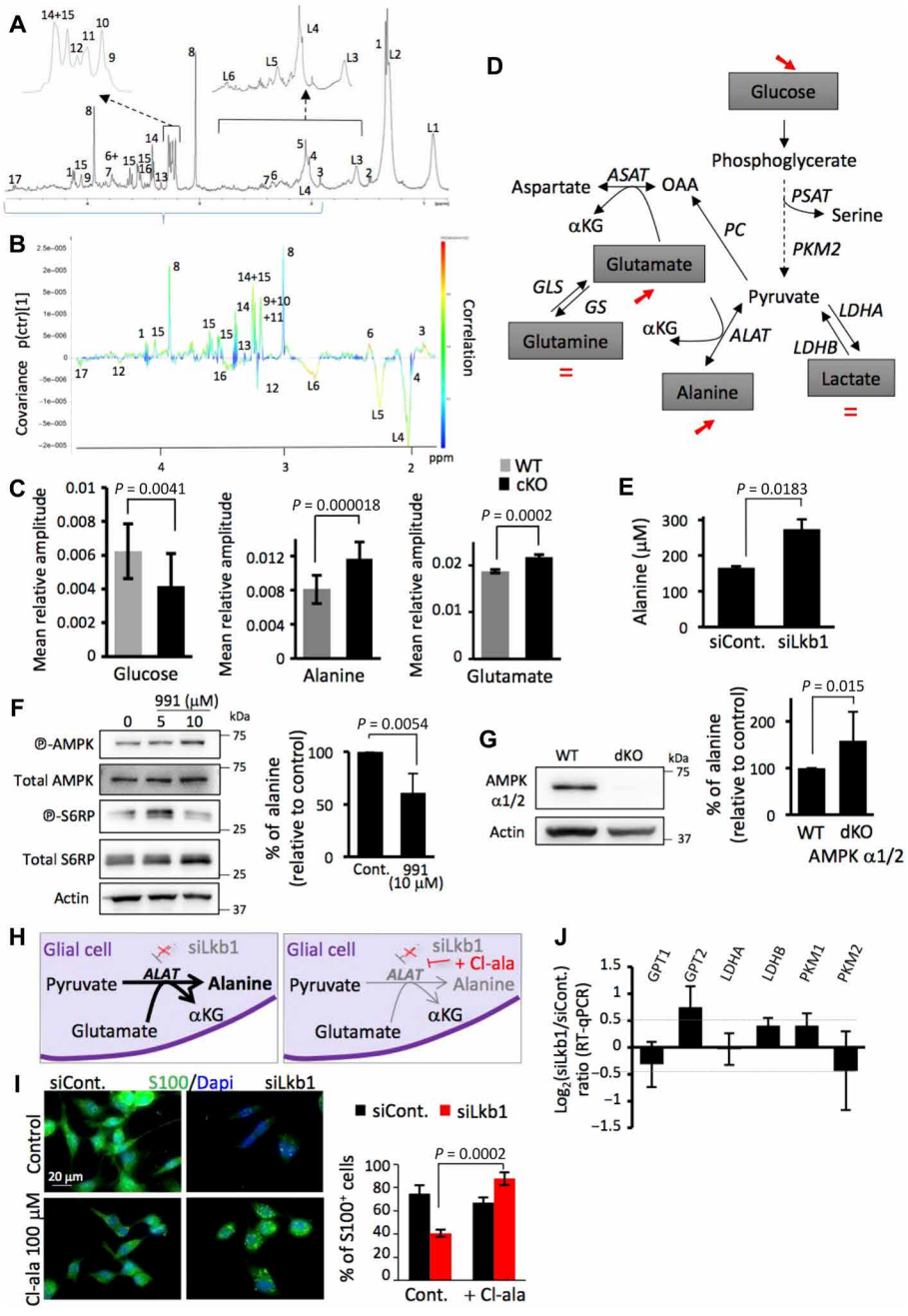

Fig. 4. Lkb1 loss in sciatic nerves triggers a metabolic reprogramming. (**A**) ^{1}H HRMAS NMR spectrum of the two sciatic nerves of a cKO mouse. Insets showing lipid and macromolecule peaks. (**B**) Zoom on small metabolites from (A) (blue bracket). Loadings of the predictive component of the multivariate statistical model built with spectral buckets of WT and cKO mouse spectra for identification of up-regulated (positive) and down-regulated (negative) metabolites in cKO mice. The loading plots are colored according to variable importance to the projection, and some assignments are indicated. Glucose, glutamate, alanine, and lipid peaks have the highest correlation value. (**C**) Mean relative amplitude of glucose [$d = 4.65$ parts per million (ppm)], alanine ($d = 1.48$ ppm), and glutamate ($d = 2.35$ ppm) peaks in each mouse group relative to trimethylsilylpropionate (TSP) at 0 ppm. (**D**) Schematic representation of metabolic pathways illustrating the defects observed by metabolomics profiling on sciatic nerves upon *Lkb1* ablation. αKG, α-ketoglutarate; OAA, oxaloacetate; ALAT, alanine aminotransferase; ASAT, aspartate aminotransferase; GLS, glutaminase; GS, glutamine synthetase; LDHA/B, lactate dehydrogenase A/B; PC, pyruvate carboxylase; PKM2, pyruvate kinase M2; PSAT, phosphoserine aminotransferase. (**E**) Intracellular alanine concentration of control (siCont.) or *Lkb1* knockdown (siLkb1) glial JoMa1.3 cells ($n = 3$). (**F**) Western blot (left) showing decreased mTORC1 activity in WT MEF treated with 10 μM of the AMPK agonist 991. Alanine concentration (represented as percentage relative to control) is shown on the right ($n = 4$). (**G**) Western blot validating MEF WT and double knockout (dKO) for AMPKα1/2 (left). Alanine concentration (percentage relative to control) is shown (right, $n = 6$). (**H**) Schematic representation of metabolic reprogramming triggered by *Lkb1* silencing (siLkb1, left) or by ALAT inhibition with chloroalanine inhibitor (Cl-ala; right) concomitant to siLkb1. (**I**) Glial differentiation assessed by S100 immunostaining of JoMa1.3 cells upon chloroalanine treatment. Representative images (left) and quantification (right) of the percentage of S100-positive cells ($n = 3$). (**J**) RT-qPCR showing expression of metabolic genes in glial JoMa1.3 cells upon *Lkb1* silencing. *GPT1, 2*, glutamic pyruvate transaminase (encoding ALAT1, 2). Data are expressed as relative expression in control cells compared to siLkb1 cells (siCont./siLkb1). Only *GPT2* expression is slightly enriched in siLkb1-treated cells ($n = 4$).

either cytoplasmic (ALAT1) or mitochondrial (ALAT2). To address this question, ALAT enzymatic activity was blocked using the inhibitor β-chloro-L-alanine (chloroalanine) (Fig. 4H, right) (*35*). The alanine level was normalized upon *Lkb1* knockdown, thus demonstrating that chloroalanine is a genuine inhibitor of ALAT in glial JoMa1.3 cells (fig. S7I). We also measured lactate levels and observed that *Lkb1* knockdown resulted in a decrease of lactate concentration, whereas chloroalanine treatment led to an increase of lactate level (fig. S7J). Therefore, *Lkb1* silencing induced a preferred conversion of pyruvate into alanine rather than to lactate. To examine the relation of the pyruvate/alanine transformation with glycolysis, we measured medium acidification due to the excretion of both lactate and proton using the Seahorse analyzer. The basal glycolysis and glycolytic capacity were slightly reduced, while the glycolytic reserve was markedly diminished in the absence of *Lkb1* (fig. S7K). However, upon ALAT inhibition with chloroalanine, the extracellular pH of cells with or without *Lkb1* was similar, thus demonstrating that glycolysis was not affected (fig. S7L). These data thus support the idea that the pyruvate is preferentially transformed into alanine upon *Lkb1* knockdown independently of the glycolytic rate. We next evaluated the ability of cells to be specified into the glial lineage upon both *Lkb1* knockdown and ALAT inhibition. Chloroalanine treatment of *Lkb1*-knockdown cells led to a drastic reduction of actin stress fiber formation (fig. S7M) and rescued expression of the glial marker S100 (Fig. 4I).

Analyses of the expression of a set of genes coding for metabolic enzymes during glial differentiation showed that progenitor cells expressed, at a higher level, the genes coding for lactate dehydrogenase A (*LDHA*) and pyruvate kinase M2 (*PKM2*), whereas glial cells had enriched expression of lactate dehydrogenase B (fig. S7N). LDHA and PKM2 are associated with cell proliferation (*36*), and their enriched expression in progenitor cells fits with the neural crest stem phenotype of JoMa1.3 cells. However, *Lkb1* knockdown did not drastically change the expression levels of these metabolic genes (Fig. 4J). However, with a low threshold (over −0.5 or 0.5), we observed that *GPT2* expression, which encodes the mitochondrial form of ALAT, was enriched in glial cells upon *Lkb1* knockdown, thereby suggesting that alanine accumulation is linked to an elevated expression of *GPT2*.

Alanine production controls glial cell fate in an mTOR-dependent manner

The LKB1-AMPK signaling pathway suppresses the function of the mTORC1, an essential regulator of protein synthesis, growth, and metabolism (*37*). Consistent with this function, the phosphorylation of the S6 ribosomal protein (S6RP), a substrate of the p70S6 kinase acting downstream of mTORC1, was enhanced in the enteric ganglia of intestine and colon regions of cKO mice as well as in the sciatic nerves (Fig. 5, A and B). We also observed an activation of the mTORC1 pathway in JoMa1.3 progenitor and glial cells upon *Lkb1* knockdown (Fig. 5C). Conversely, a substantial decrease of mTORC1 was detected upon chloroalanine treatment (Fig. 5D), suggesting that this kinase acts downstream of the pyruvate-alanine pathway.

To evaluate the connection between alanine levels, mTORC1 activity, and glial differentiation, we cultivated JoMa1.3 cells in glial differentiation conditions with increasing doses of alanine. We first validated that alanine accumulated in glial cells (fig. S8A). In these conditions, mTOR activity was up-regulated (fig. S8B) and glial differentiation was impaired (fig. S8C), thus recapitulating the effects of *Lkb1* knockdown in glial cells. To explore if alanine levels are essential to maintain stemness, we treated JoMa1.3 progenitor cells with the ALAT inhibitor chloroalanine. This treatment decreased basal levels of alanine (fig. S8D) and limited mTORC1 activity (fig. S8E). However, ALAT inhibition in progenitors did not trigger any "by default" glial differentiation (fig. S8F). Together, these data highlight the interconnected regulation of alanine biosynthesis and mTORC1 activity and demonstrate that alanine levels are essential for glial differentiation.

Because our data hinted at a mechanistic link between the sensing of alanine levels and mTOR activity, we treated *Lkb1* knockdown JoMa1.3 cells with the mTOR inhibitor Torin1. As expected, Torin1 normalized mTOR activation in JoMa1.3 cells silenced for *Lkb1* (Fig. 5E). Immunofluorescence staining with the glial marker S100 revealed that Torin1 treatment rescued glial differentiation of *Lkb1*-deficient cells (Fig. 5F). These data provide evidence that Lkb1 controls glial cell differentiation through the regulation of alanine synthesis that acts upstream of mTOR.

Reduced mitochondrial respiration does not affect glial differentiation

LKB1 and AMPK play a crucial role in controlling mitochondrial activity (*25*, *26*, *38*–*40*). Therefore, we assessed whether the inhibition of glial differentiation caused by *Lkb1* inactivation was associated with mitochondrial defects. After labeling cells with MitoTracker, a vital stain that accumulates in active mitochondria, mitochondria of cKO sciatic nerves appeared more dispersed in myelinated fibers compared to WT littermates (Fig. 6A). Electron microscopy showed dilated mitochondrial cristae in the absence of *Lkb1* (Fig. 6B). Using MitoTracker staining and flow cytometry analyses in JoMa1.3 cells, a significant increase of the mitochondrial mass was observed (Fig. 6C). Confocal microscopy analyses revealed a marked reorganization of the mitochondria network that acquired a large circular morphology (Fig. 6D). Next, we assessed the respiratory capacities of *Lkb1*-deficient glial JoMa1.3 cells and found a significant diminution of oxygen consumption during basal, maximal, and spare respiration. Adenosine 5′-triphosphate (ATP) production was also significantly reduced (Fig. 6E). However, chloroalanine treatment did not rescue the mitochondrial respiration (Fig. 6F), thus indicating that reduced oxygen consumption in our system is not linked to the inhibition of glial differentiation.

AICAR rescues glial differentiation and prevents in vivo NCC defects

The AICAR compound is phosphorylated by adenosine kinase inside the cells and is converted to purine nucleotides, among them 5-aminoimidazole-4-carboxamide ribotide (AICA ribotide or ZMP) and AMP, two allosteric activators of AMPK (*41*). Although AICAR has been described as an AMPK agonist in the presence of Lkb1, there is increasing evidence that this molecule exerts AMPK-independent metabolic effects (*42*–*44*). Furthermore, AICAR supplementation promotes astroglial differentiation independently of AMPK (*44*). These data prompted us to test whether AICAR could rescue glial differentiation of *Lkb1*-deficient NCC derivatives. AICAR treatment decreased actin stress fiber formation (fig. S9A) and rescued S100 expression (Fig. 7A). AICAR had no effect on alanine levels (fig. S9B); however, it significantly diminished mTORC1 activation without restoring AMPK phosphorylation (Fig. 7B). Notably, AICAR treatment affected neither mitochondrial respiration (fig. S9C) nor glycolysis

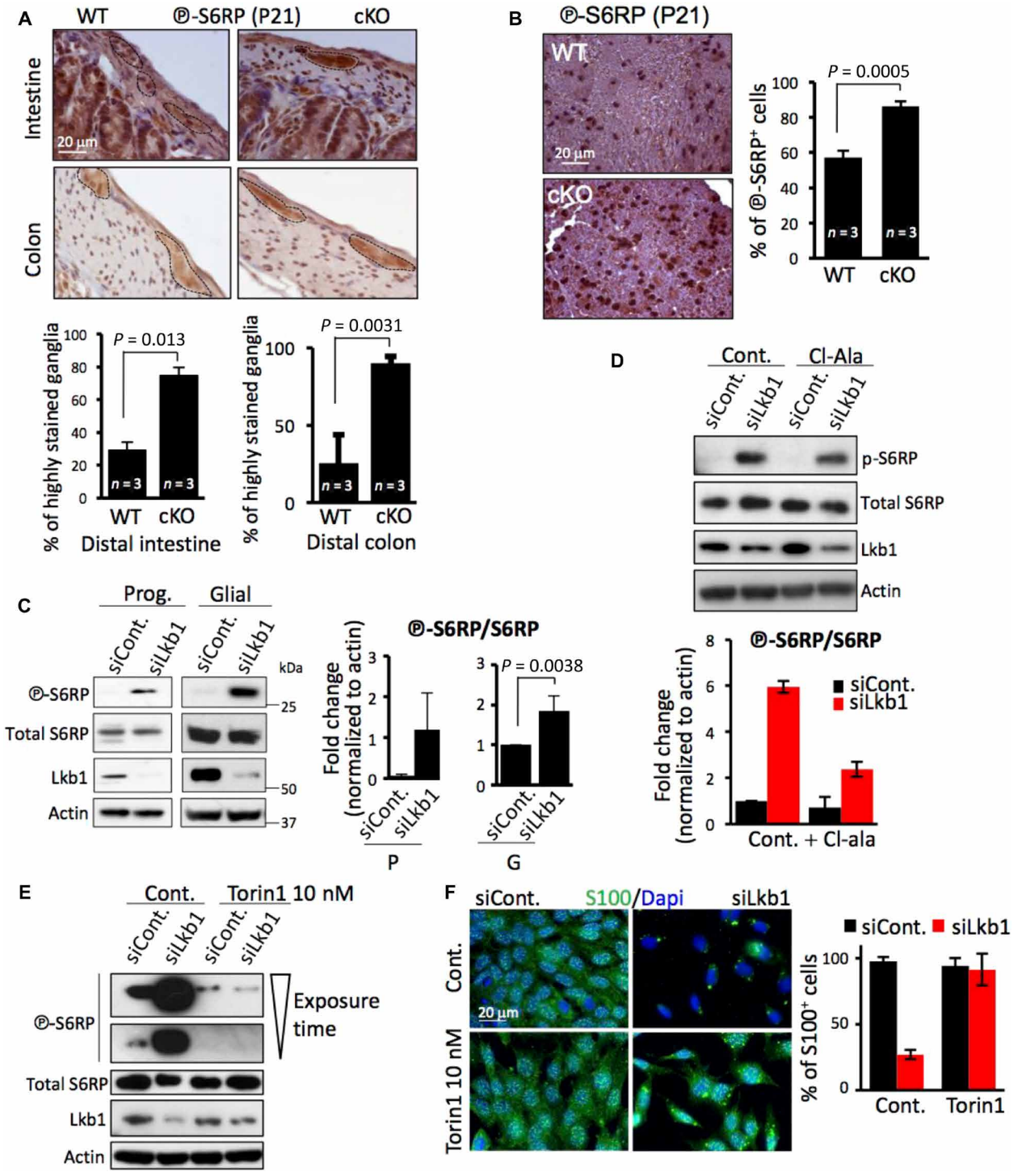

Fig. 5. Up-regulation of mTORC1 correlates with deregulated alanine levels upon Lkb1 loss. (**A**) Increased phospho-S6RP staining was observed in cKO animals in both the intestine and colon. Myenteric ganglia are surrounded by dotted lines. The graphs below represent the percentage of highly phospho-S6RP–stained ganglia in the distal intestine and distal colon. (**B**) Increased phospho-S6RP staining was observed in cKO animals in transverse sections of sciatic nerves. Right: Quantification. (**C**) Phosphorylation of S6RP as an indicator of mTORC1 activity was assessed by Western blot and compared to total S6RP level in progenitor (P) and glial (G) JoMa1.3 cells. Actin was used as a loading control. Graphs show quantifications for progenitors (left, $n = 2$) and glial cells (right, $n = 4$). (**D**) ALAT inhibition by chloroalanine limited the up-regulation of the mTORC1 pathway. Representative Western blots (top). Quantification of phosphorylated S6RP protein relative to total S6RP protein (bottom, $n = 2$). (**E**) Torin1 is a potent mTOR inhibitor in JoMa1.3 glial cells as illustrated by a representative Western blot ($n = 2$). (**F**) mTOR inhibition by Torin1 rescues glial differentiation as shown by representative images (left) and evaluation of the percentage of S100-positive cells (right, $n = 2$).

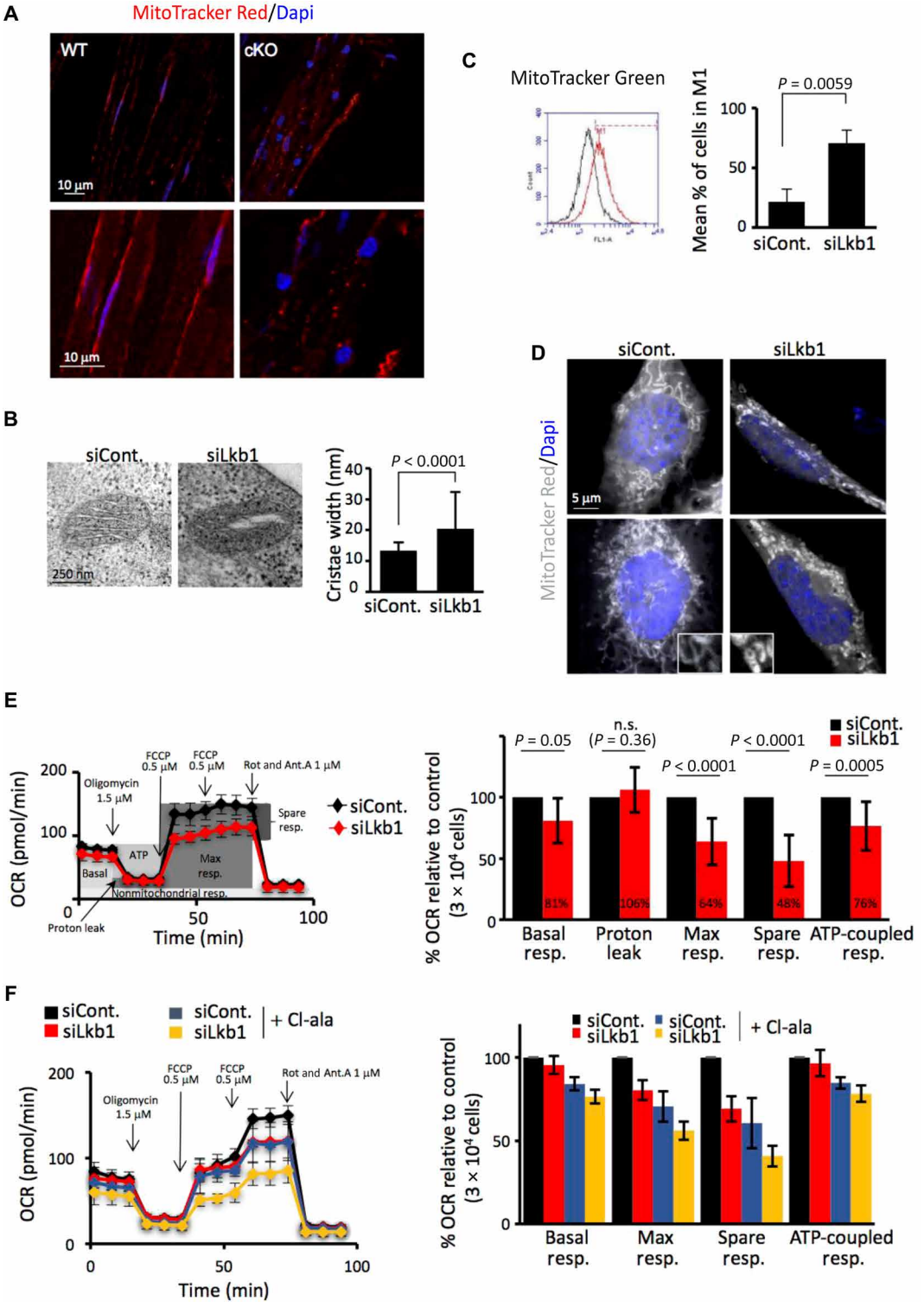

Fig. 6. Reduced mitochondrial respiration upon Lkb1 loss does not affect glial differentiation. (**A**) Confocal analyses of MitoTracker staining on isolated myelinated nerve fibers of WT or *Lkb1*-deficient mice (cKO). (**B**) Representative electron microscopy images of mitochondria from control (siCont.) and *Lkb1* knockdown (siLkb1) glial JoMa1.3 cells showing increased cristae width in the absence of *Lkb1*. Quantification was performed on 429 and 336 cristae from mitochondria of control and *Lkb1*-silenced cells, respectively. (**C**) Mitochondrial mass was quantified by fluorescence-activated cell sorting analyses with MitoTracker Green staining ($n = 3$). (**D**) Mitochondrial topology of glial JoMa1.3 cells stained with MitoTracker Red was analyzed by confocal microscopy ($n = 3$). (**E**) Representative trace showing change in oxygen consumption rates (OCRs) during a mitochondrial stress assessed by Seahorse analyses on control (siCont.) and *Lkb1*-silenced (siLkb1) glial JoMa1.3 cells. Right: Quantification ($n = 12$). (**F**) Representative curves showing change in oxygen consumption (OCR, left) upon chloroalanine treatment. Right: Quantification of % OCR relative to control cells (siCont. with the control condition of treatment) ($n = 4$). Ant.A, antimycin A; FCCP, carbonyl cyanide *p*-trifluoromethoxyphenylhydrazone; Rot, rotenone.

(fig. S9D). Together, these findings suggest that AICAR rescued *Lkb1* loss by acting downstream of alanine biosynthesis and upstream of mTORC1.

We next explored the in vivo effects of AICAR on *Lkb1* cKO mice. *Lkb1*-deficient mice were treated by intraperitoneal injections of AICAR (0.5 mg/g body weight) every 2 days from P10 to P18. We first observed that weight loss of cKO animals was reduced upon AICAR infusion (Fig. 7C). Furthermore, at P21, mutant mice treated with AICAR displayed increased mobility and ameliorated leg reflex extension when lifted by their tail compared to mutant mice treated with vehicle (Fig. 7D). In addition, P21 mutant mice showed less intestinal dilation (Fig. 7E). As observed in vitro, AICAR also limited in vivo mTOR up-regulation due to *Lkb1* loss. Inhibition of mTORC1 signaling was restored both in sciatic nerves (Fig. 7F) and in the enteric nervous system (Fig. 7G). Strikingly, neuronal and glial enteric cells were maintained in mutant mice with AICAR (Fig. 7H). Thus, AICAR rescued, at least in part, enteric and Schwann cell defects of cKO mice.

DISCUSSION

Multipotent NCCs face a limiting supply of oxygen and nutrients during their journey through the embryo and the distant colonization of organs. The metabolic adaptation of NCC to these microenvironmental conditions constrains their migration, proliferation, differentiation, and survival. However, the metabolic pathways that are involved in the formation of neural crest derivatives have remained poorly characterized. We show here that the tumor suppressor kinase LKB1 is a key effector in an NCC metabolic program that drives melanocyte and glial cell differentiation.

Disruption of *Lkb1* in the subpopulation of NCC expressing tyrosinase impaired the differentiation of melanocytes, enteric ganglion cells, and Schwann cells. It has been previously reported that the combined inactivation of *Lkb1* and the oncogenic activation of *K-Ras* in melanocytes led to inappropriate melanogenesis and to the metastatic expansion of melanoma (*45*). We now establish that Lkb1 is required during the first wave of melanocytic differentiation. In addition, we found that Lkb1 activity is also necessary for the postnatal maintenance of neurons and glial cells of myenteric and submucosal plexi. However, we cannot exclude that Lkb1 also functions at earlier stages of vagal NCC migration, because NCCs invade the rostral foregut at E8.5 or E9, while the tyrosinase promoter is turned on at E10.5. Unexpectedly, we did not detect an increase of NCC apoptosis that might account for the defect in the enteric nervous system. However, apoptosis may occur at earlier stages of NCC development and went undetected in our experiments. Alternatively, an unconventional death of postmigratory enteric neurons has been described in mice with a conditional ablation of each subunit of the glial cell line–derived neurotrophic factor (GDNF) receptor, GFRα1 and RET (*46*, *47*). It might thus be interesting to explore if *Lkb1* loss affects GDNF signaling. Strikingly, Schwann cell precursors (SCPs) depend on GDNF signaling to populate the gut through extrinsic nerves (*48*, *49*). SCPs are progenitors from peripheral nerves with NCC stem-like properties that contribute to the postnatal integrity of the enteric nervous system (*50*). It is thus plausible that postnatal degeneration of the enteric nervous system occurring in *Lkb1* cKO mice reflects an attrition of the SCP pool.

Our work further revealed that NCC-specific ablation of *Lkb1* resulted in a progressive peripheral neuropathy stemming from an impaired differentiation of Schwann cells. These results are consistent with recent studies demonstrating the implication of Lkb1 in Schwann cell axon maintenance and myelination using Cnp::Cre or P0::Cre drivers (*25*–*27*). Despite the fact that our *Lkb1* mutant mice displayed phenotypic manifestations at earlier developmental stages (around 2 to 4 weeks after birth), we observed a similar disruption of Schwann cell polarization and mitochondrial activity. However, in contrast with a previous report (*26*), we found that mitochondrial respiration is not required for glial cell commitment. This discrepancy probably reflects that, in our conditions, early stages of the glial lineage were studied when the cells are still actively proliferating. Along this line of thinking, the timing of *Lkb1* inactivation likely explains why we did not observe a decrease of the level of the citrate metabolite, as previously reported in Schwann cells that lack Lkb1 (*26*). By combining in vivo, metabolomics, and pharmacological approaches, we found instead that *Lkb1* deletion led to an intracellular accumulation of alanine. Inhibition of pyruvate-alanine transamination restored glial differentiation of *Lkb1*-deficient NCC, whereas treatment of NCCs with alanine blocked their glial differentiation. We further established that AMPK is a key negative regulator of alanine biosynthesis downstream of Lkb1 (fig. S10). It has been recently demonstrated that rapidly proliferating mammary epithelial cells use transaminases to link nonessential amino acids synthesis to the production of α-ketoglutarate and tricarboxylic acid anaplerosis (*51*). Furthermore, the activation of *GPT2* expression, the gene encoding ALAT2, is required to maintain the malignant phenotype of colon cells by coupling of glycolytic flux to anaplerosis (*52*). These findings are in agreement with our data because the unchecked activation of the pyruvate-alanine cycling is incompatible with the transition of *Lkb1*-deficient NCC to quiescence and subsequent glial differentiation. *Lkb1* loss has also been associated with an increased expression of phosphoserine amino transferase, an enzyme participating to the serine-glycine one-carbon network whose aberrant activation supports the malignant transformation of *Lkb1*-mutant pancreatic cells (*53*). These data point to Lkb1 as a key actor of a metabolic checkpoint that controls a switch between cell proliferation and differentiation through transaminases-dependent alanine synthesis.

We report here that mTORC1 activation is connected to the elevated alanine level and that inactivation of mTOR signaling restored glial differentiation of Lkb1-deficient NCC. mTORC1 is known to control cranial NCCs (*54*, *55*) and early and late stages of Schwann cell differentiation, and an adequate dosage of mTOR activity is required for the peripheral nervous system myelination (*56*–*60*). In addition, in agreement with our results, mTORC1 reactivation has been associated with Schwann cell dedifferentiation during nerve injury (*61*). Although we have explored the link between alanine and mTORC1 in glial differentiation, we cannot rule out the involvement of mTORC2 in this process. mTORC1 is stimulated in response to the sensing of amino acids in particular leucine and arginine (*62*). However, additional amino acids are presumably involved in this process (*63*, *64*). In support of this notion, it has been recently demonstrated that mTORC1 is activated in two consecutive priming and activation steps (*65*) and that alanine belongs to the group of priming amino acids. These findings suggest a rational mechanistic explanation supporting our data, and it will thus be relevant to investigate how alanine sensing might be tied to the activation of mTORC1.

In this context, it was an unexpected observation that the treatment of *Lkb1*-deficient NCC with the cell-permeable nucleoside AICAR normalized mTORC1 signaling both in vitro and in vivo without

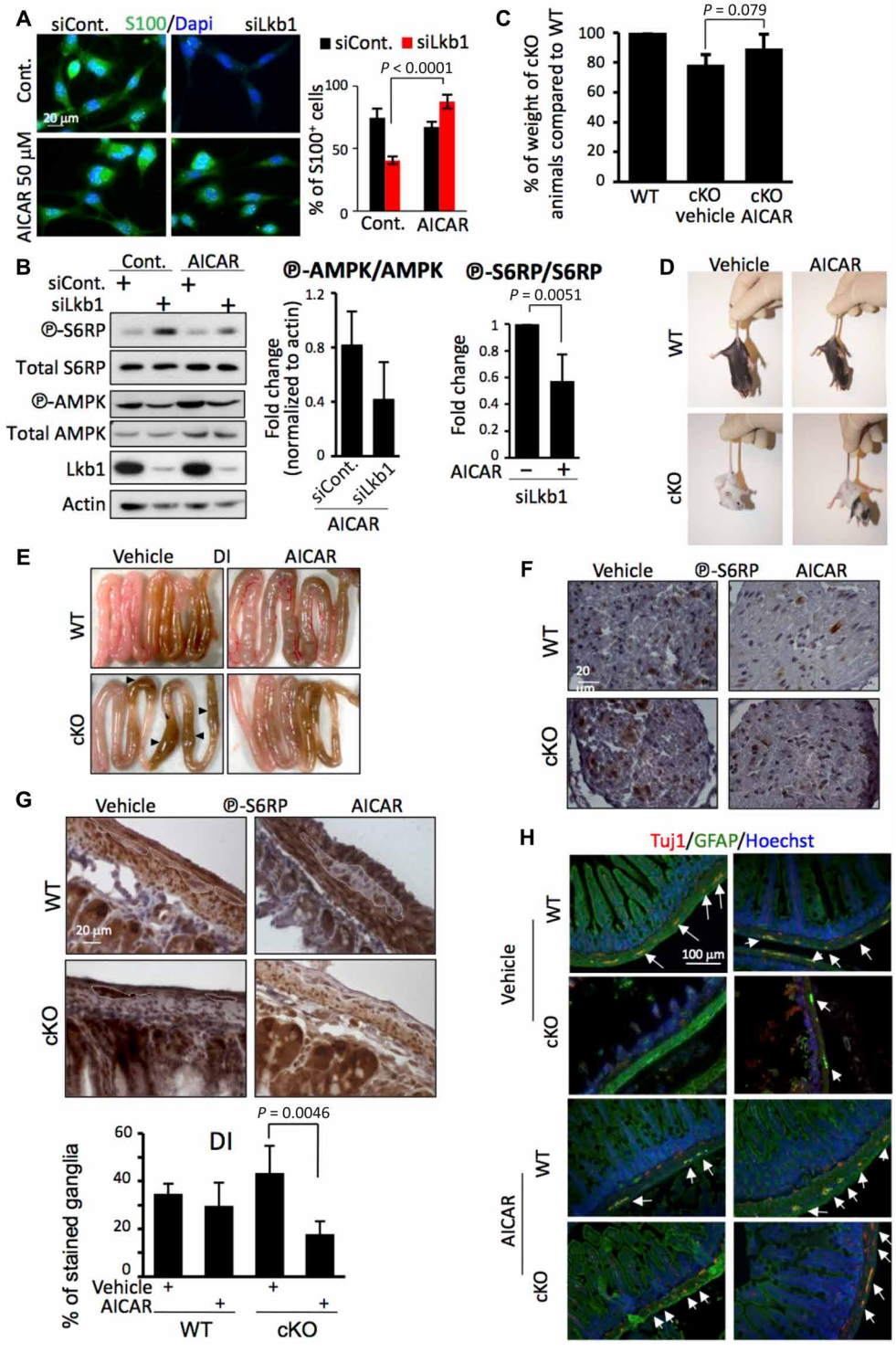

Fig. 7. AICAR treatment rescues glial differentiation in vitro and prevents neural crest defects in vivo. (**A**) Impaired glial differentiation visualized with the S100 glial marker due to *Lkb1* knockdown was rescued by AICAR treatment of JoMa1.3 cells. Right: Percentage of S100-positive cells ($n = 3$). (**B**) Western blot showing that AICAR treatment does not rescue AMPK activation but normalizes mTORC1 activity. Quantifications are shown (left graph for AMPK, $n = 2$; right graph for S6RP, $n = 4$). (**C** to **E**) Injection of *Lkb1*-deficient animals intraperitoneally from P10 to P18 with the AMP analog AICAR partly rescued weight loss (C), improved hind limb extension reflex (D), and prevented intestinal dilation (E). (**F** and **G**) AICAR treatment of cKO mice rescued mTORC1 inhibition compared to vehicle-treated cKO animals in both sciatic nerves (F) and enteric nervous system (G). Myenteric ganglia are surrounded by dotted lines. Graph in (G) represents the percentage of phospho-S6RP–stained ganglia in the distal intestine. (**H**) The integrity of the intestinal villi and the number of enteric neurons (red) and glial cells (green) are rescued in AICAR-treated mice. Arrows point to enteric ganglia. Representative pictures from two different animals are shown (left and right pictures for each condition). $n = 5$ mice per condition. Photo credits: Sakina Torch and Chantal Thibert, University Grenoble Alpes.

restoring AMPK phosphorylation and promoted glial differentiation in vitro. AICAR is mostly known to exert its biological effects through AMPK, although it has become progressively evident that this metabolite has additional cellular targets (*66*). Recent reports showed that AICAR acts in an AMPK-independent manner either on mTOR inhibition or on the Nrf2 pathway (*67*, *68*). The remarkable rescue of hind limb paralysis and enteric nervous system degeneration obtained with AICAR indicates that this compound or molecules up-regulating its intracellular level (*69*) may represent a viable therapeutic intervention to target the metabolic defects induced by *LKB1* inactivation.

Collectively, this study and our previous report (*18*) identify the LKB1 pathway as a central orchestrator of neural crest development and highlight the pivotal role of energy metabolism in the formation of NCC lineages. These findings also raise the idea that a dysfunctional LKB1 signaling network could underlie the metabolic etiology of human neurocristopathies including peripheral neuropathies and intestinal motility disorders.

METHODS

Animals and genotyping

Floxed *Lkb1* mice were obtained from R. A. DePinho (Boston, USA), and R26R mice were provided by P. Soriano (New York, USA). Characterizations of *Lkb1 Floxed* (*19*), *Tyr::Cre* (*20*, *21*), and *R26R* (*23*) mice have been reported previously. Because *Tyr::Cre* transgene is located on the X chromosome, to avoid a bias due to X chromosome inactivation, our study is solely based on the analysis of males. Heterozygous $Lkb1^{+/F}$;$Tyr::Cre^{+/tg}$ male mice were fully healthy and fertile. Heterozygous ($Lkb1^{+/F}$) and homozygous ($Lkb1^{F/F}$) males were crossed with $Lkb1^{+/F}$ $Tyr::Cre^{+/tg}$ females to generate *Lkb1* homozygous conditional knockout in neural crest–derived tissues (referred to as cKO in the text) and WT littermate animals in a mixed genetic background, mostly C57BL6/J (WT: $Lkb1^{+/F}$, $Lkb1^{F/F}$, and $Lkb1^{+/+}$;*Tyr::Cre* male mice). Embryos and mice were genotyped by multiplex polymerase chain reaction (PCR) using DNA extracted from tails with primers indicated in Table 1 and PCR conditions in original references cited previously. For timed pregnancies, mice were bred and the time of plug identification was counted as day 0.5. Mice were maintained under standard housing conditions at the animal facility Plateforme Haute Technologie Animalerie (PHTA) of Grenoble and on a mixed genetic background. $Tyr::Cre^{+/tg}$;$Z/EG^{+/tg}$ mice were described previously (*28*, *70*). All animal experimental procedures were conducted according to the standard operating procedures of the laboratory animal facility and were approved by the Animal Ethics Committee of Grenoble (permit no. 261_ IAB-U823-CT-01).

Human samples

Normal human intestine and colon tissue samples were obtained from biopsies of patients with peritoneal intestinal carcinosis. All samples collected were taken at distance from the bulk of the tumor, stored, and used with the informed consent from the patients.

Cell culture conditions, siRNA transfection, and metabolic drug treatments

Lkb1 null mouse immortalized embryonic fibroblasts or reconstituted to express *Lkb1* were cultivated as previously described (*71*). Culture of mouse immortalized embryonic fibroblasts WT or double knockout for *AMPKα1/2* was performed as previously described (*72*).

Mouse immortalized neural crest stem cells (JoMa1.3) were cultured on fibronectin (10 μg/ml; 1 hour at 37°C)–coated surfaces following the protocol described by Maurer *et al.* (*34*). Differentiation of these cells into glial cells was achieved by coating surfaces with poly-L-lysine (10 μg/ml; 1 hour at 37°C) and fibronectin and by adding heregulin (50 ng/ml; PeproTech,120-02) and forskolin (5 μM; Sigma) to the culture medium for 6 days. The medium was replaced every 2 days.

siRNAs against the mouse *Lkb1* gene and the nontargeting control siRNA were purchased from Dharmacon (ON-TARGETplus Mouse Stk11 SMART Pool and ON-TARGETplus Non-targeting Pool). siRNAs were first transfected (60 nM) into JoMa1.3 progenitor cells (2×10^4 cells/ml) by using jetPRIME (Ozyme) according to the manufacturer's protocol. For nondifferentiated JoMa1.3 cells, experiments were performed 72 hours after transfection. For differentiated JoMa1.3 cells, 3 days after the first transfection, cells were redistributed (2×10^4 JoMa1.3 cells/ml) and transfected again 48 hours later. Thus, two cycles of 96 hours of *Lkb1* knockdown were performed, as described in fig. S4E.

During the 6 days of cell differentiation and the second cycle of *Lkb1* inactivation, cells were cultivated in NCC medium and replaced every 2 days from days 4 to 9 and supplemented when indicated with different metabolic inhibitors: 100 μM chloroalanine (ALAT inhibitor; Sigma), 10 nM Torin1 (an mTOR inhibitor; Euromedex), and 50 μM AICAR (a metabolic regulator and AMPK agonist; Millipore).

For alanine supplementation experiments, JoMa1.3 cells (seeded at 2×10^4 cells/ml) were supplemented with alanine during 4 or 5 days in glial differentiation medium and replaced every 2 days. When indicated, cells were treated with Torin and AICAR as described above.

Electron microscopy

For electron microscopy, mice were anesthetized with ketamine/xylazine and perfused with 2% paraformaldehyde and 0.2% glutaraldehyde in phosphate-buffered saline (PBS) (0.1 M, pH 7.4), and dissected sciatic nerves were fixed with 2% paraformaldehyde and 2.5% glutaraldehyde in PBS (0.1 M, pH 7.4) for 1 hour at room temperature and post-fixed in 1% osmium tetroxide in cacodylate buffer (0.1 M, pH 7.2) for 1 hour at 4°C. After washing, tissues were stained in 0.5% uranile acetate (pH 4) for 1 hour at 4°C, then dehydrated through graded alcohols, and embedded in Epon. Semithin sections (500 nm) were stained with toluidine blue before being observed with an optical microscope. Ultrathin sections (50 nm) were analyzed with a transmission electron microscope (JEOL 1200EX, Grenoble Institute of Neurosciences, France) at 80 kV, and images were acquired using a digital camera (Veleta, Olympus). Morphometric measurements were done with ITEM software (Soft Imaging System, Olympus). The same protocol was applied for electron microscopy on JoMa1.3 cells.

Teased fiber preparation and staining

Sciatic nerves were isolated from WT or cKO mice, teased on glass slides, fixed for 30 min in 4% paraformaldehyde, and subsequently washed in PBS (*73*). After teasing, the nerves were dried overnight at room temperature and stored at −20°C. For E-cadherin immunostaining, the teased fibers were permeabilized in cold acetone for 10 min, washed with PBS, incubated for 1 hour at room temperature in blocking solution (10% goat serum and 0.3% Triton X-100 in PBS), and then incubated with primary antibodies in blocking solution overnight at 4°C. Samples were washed in PBS and incubated for 1 hour at room temperature with secondary antibodies. Last, samples were washed in PBS incubated

Table 1. Primers used for genotyping and qPCR. bp, base pair.

Genotyping PCR	Primer sequences	Band size
Cre	Cre5: 5′-CCTGGAAAATGCTTCTGTCCGTTTGCC-**3′** Cre3: **5′**-GAGTTGATAGCTGGCTGGTGGGAGATG-**3′**	654-bp Cre allele
Lkb1	Lkb1–55: **5′**-TCTAACAATGCGCTCATCGTCATCCTCGGC-**3′** Lkb1–36: **5′**-GGGCTTCCACCTGGTGCCAGCCTGT-**3′** Lkb1–39: **5′**-GAGATGGGTACCAGGAGTTGGGGCT-**3′**	220-bp WT allele 300-bp Flox allele
R26R	R26RGT1: **5′**-AAAGTCGCTCTGAGTTGTTAT-**3′** R26RGT2: **5′**-GCGAAGAGTTTGTCCTCAACC-**3′** R26RGT3: **5′**-GGAGCGGGAGAAATGGATATG-**3′**	500-bp WT allele 250-bp Flox allele
qPCR	**Primer sequences**	**Band size**
AUP1	mAUP1-F: **5′**-tgcgctccgtgtacaacagc-**3′** mAUP1-R: **5′**-tttgtcgcttcatgtgttct-**3′**	95 bp
RELA	mRELA-F: **5′**-cgggatggctactatgagg-**3′** mRELA-R: **5′**-ctccaggtctcgcttctt-**3′**	96 bp
cMyc	mcMyc-F: **5′**-gcctagaattggcagaaatga-**3′** mcMyc-R: **5′**-aactgagaagaatcctattcagcac-**3′**	130 bp
Lkb1	mLkb1-F: **5′**-CTCCGAGGGATGTTGGAGTA-**3′** mLkb1-R: **5′**-GCTTGGTGGGATAGGTACGA-**3′**	119 bp
Sox10	mSox10-F: **5′**-AGATCCAGTTCCGTGTCAATAA-**3′** mSox10-R: **5′**-GCGAGAAGAAGGCTAGGTG-**3′**	136 bp
p75^{NTR}	mp75-F:**5′**-ATGGATCACAAGGTCTACCCC-**3′** mp75-R:**5′**-GGAGCAATAGACAGGAATGAGG-**3′**	190 bp
S100B	mS100B-F: **5′**-tgaaggagcttatcaacaacga-**3′** mS100B-R: **5′**-tccatcactttgtccaccac-**3′**	79 bp
Gpt1	mGPT1-F:**5′**-GGTGCTAACTCTGGATAC-**3′** mGPT1-R:**5′**-TGGCACGGATAACCTCAG-**3′**	143 bp
Gpt2	mGPT2-F:**5′**-atgtgaaggctgtggagtaagg-**3′** mGPT2-R:**5′**-ctgcagtgtgggactataggg-**3′**	60 bp
LdhA	mLDHA-F:**5′**-ggcactgacgcagacaag-**3′** mLDHA-R:**5′**-tgatcacctcgtaggcactg-**3′**	73 bp
LdhB	mLDHB-F:**5′**-acaagtgggtatggcatgtg-**3′** mLDHB-R:**5′**-acatccaccagggcaagtt-**3′**	72 bp
Pkm1	mPKM1-F:**5′**-cgcatgcagcacctgata-**3′** mPKM1-R:**5′**-caaacagcagacggtgga-**3′**	61 bp
Pkm2	mPKM2-F: **5′**-aaggggactaccctctgg-**3′** mPKM2-R:**5′**-cctcgaatagctgcaagtgg-**3′**	91 bp

in Hoechst to stain nuclei and mounted in Mowiol. Images were acquired using a Zeiss Biphoton confocal microscope (LSM510).

To label mitochondria, teased fibers were incubated with MitoTracker Red CMX-ROS (Invitrogen) for 30 min at 37°C (500 nM), washed in PBS, fixed for 10 min in 4% paraformaldehyde, incubated in Hoechst for 10 min, and mounted in Mowiol. Images were acquired using a Zeiss Biphoton confocal microscope (LSM510).

Seahorse analyses

The extracellular acidification rate (ECAR) and O_2 consumption rate (OCR) were analyzed using the Seahorse XF-Analyzer (Seahorse Bioscience), and 3×10^4 cells were seeded in 96-well Seahorse plates in glial JoMa1.3 culture medium for 16 hours before assay. Cells were equilibrated with DMEM lacking bicarbonate at 37°C for 1 hour in a custom incubator without CO_2. OCR and ECAR were measured at baseline following addition of reagents for indicated times. For the mitochondrial respiration, the spare respiratory capacity was calculated by subtracting the maximal respiration values by the basal respiration values. For both respiration and glycolysis, quantifications were performed by calculating for each category the mean and SD from the values obtained from several independent experiments.

Biochemical dosages

Metabolites were quantified from 10^7 JoMa1.3 cells using the Alanine Assay Kit (BioVision, K652-100), Citrate Assay Kit (BioVision, K655-100), and Lactate Assay Kit (BioVision, K2092-100) according to the manufacturer's protocols.

AICAR treatment of mice

WT and cKO mice were treated with AICAR (0.5 mg/g body weight) or vehicle by intraperitoneal injection (100 µl per mouse) every 2 or

3 days from P10 to P18. Mice received five injections and were sacrificed at P21 and analyzed as described previously.

Graphical representations and statistical analyses

All cell culture experiments were realized at least by three independent experiments, and for one experiment, each condition was performed in triplicate. In vivo analyses were conducted with at least three animals per condition. The exact number of experiments is indicated in the figures or in the legends. Values are given as mean with SD. Normality of the data was checked with the *F* test. The unpaired Student's *t* test was used to generate *P* values for selected pairwise comparisons, and $P < 0.05$ was considered significant.

Nerve metabolomic profiling by HRMAS NMR

Sciatic nerves from 16 WT mice and 13 cKO animals were rapidly dissected at p21, cleaned of surrounding fat and connective tissues, and immediately frozen in liquid nitrogen. Left and right nerves of each animal were inserted in a disposable insert for HRMAS NMR spectroscopy in a −20°C cooling chamber.

Sample preparation for HRMAS NMR

Seven microliters of D_2O containing trimethylsilylpropionate (TSP; 1 mM) as chemical shift internal standard [0 parts per million (ppm)] was added to the sample in the disposable insert, which was sealed and inserted in a 80-µl zirconium rotor.

^{1}H HRMAS NMR acquisition

^{1}H NMR spectra were acquired with a Bruker Avance III 500 spectrometer (Bruker BioSpin, Wissembourg, France) (CEA-Grenoble and IRMaGe facility). Samples were spun at 4000 Hz, and temperature was maintained at 4°C for all experiments. One-dimensional spectra were acquired with a Carr-Purcell-Meiboom-Gill pulse sequence synchronized with the spinning rate (interpulse delay, 250 µs; total spin echo time, 30 ms). The acquisition of one ^{1}H NMR spectrum consisted of 512 scans lasting 32 min. Residual water signal was presaturated during the 1.5-s relaxation delay time.

Spectra preprocessing

All preprocessing steps were performed using the TopSpin 3.1 Bruker software (Bruker BioSpin, Karlsruhe, Germany). Spectra were aligned to the TSP signal at 0 ppm and phase-corrected. A five-order polynomial was systematically applied for baseline correction.

All spectra from 4.678 to 0.60 ppm were divided into intervals or buckets equal to 10^{-3} ppm using the AMIX software (Bruker). Each bucket was normalized to total spectrum amplitude. Because this procedure can mask minor peak variations when very intense peaks are present in the spectra, e.g., lipid peaks (L2 peak; Fig. 4A), we also performed bucketing on a reduced spectral region starting from 1.825 ppm (Fig. 4A, into brackets). Resonance assignment was performed as previously described [for metabolites: (*74*, *75*); for lipids: (*76*, *77*)].

Multivariate statistical analysis

Buckets were then imported into SIMCA v13 software (Umetrics AB, Umea, Sweden) for multivariate statistical analysis. Buckets were mean-centered, scaled to unit variance (i.e., weighted by 1/SD for a given variable), and submitted to a principal components analysis (PCA) to ensure good homogeneity of data and possibly to exclude outliers. For this aim, data were visualized by score plots, where each point represents an NMR spectrum and thus a sample. Supervised analyses like orthogonal partial least square discriminatory analyses (OPLS-DA) were thus performed using the group belonging (control or exposed) as *Y* matrix. The number of components was determined using the cross-validation procedure that produces R^2Y and Q^2 factors (>0.5). Moreover, the reliability of our OPLS-DA model was assessed by a CV-ANOVA (cross-validated analysis of variance) test. The results were visualized by plotting the score of individuals relative to the first two components of the model. To highlight metabolites that are the most discriminating between controls and exposed, S-line was examined. This plot allows the visualization in a single graph, which mimics an NMR spectrum, the covariance (peak intensity), and correlation (peak color) between cKO and WT animals. Moreover, the signs of peaks in S-line give indications about the direction of change of metabolites—increased (positive peaks) or decreased (negative peaks) relative to WT.

SUPPLEMENTARY MATERIALS

Supplementary material for this article is available at http://advances.sciencemag.org/cgi/content/full/5/7/eaau5106/DC1

Supplementary Methods

Table S1. Antibodies used throughout the study.

Table S2. Sampling used for quantifications in the enteric nervous system.

Table S3. Sampling used for quantifications in the sciatic nerves.

Fig. S1. Conditional ablation of Lkb1 in NCCs causes hypopigmentation, hind limb paralysis, and intestinal pseudo-obstruction.

Fig. S2. Lkb1 inactivation impairs melanocyte formation.

Fig. S3. Lkb1 inactivation in neural crest–derived enteric cells triggers neurodegeneration.

Fig. S4. Defective myelination of sciatic nerves in Lkb1 cKO mice correlates with defects in maturation of Schwann cells.

Fig. S5. Lkb1 loss triggers a lack of progenitor differentiation.

Fig. S6. Validation of the neural crest stem cell line JoMa1.3.

Fig. S7. Lkb1 loss rewires glial cell metabolism but does not affect glycolysis.

Fig. S8. Alanine biosynthesis and mTORC1 activity are connected in glial cells.

Fig. S9. AICAR rescues glial differentiation independently of alanine levels, mitochondrial respiration, or glycolysis.

Fig. S10. Schematic model depicting the antagonistic regulation of alanine production by LKB1/AMPK and the postulated mechanistic integration of the signal on mTOR and the tricarboxylic acid.

References (*78*–*81*)

REFERENCES AND NOTES

1. N. Le Douarin, C. Kalcheim, The neural crest, in *Developmental and Cell Biology Series* (Cambridge Univ. Press, ed. 2, 1999).
2. R. Mayor, E. Theveneau, The neural crest. *Development* **140**, 2247–2251 (2013).
3. M. C. Simon, B. Keith, The role of oxygen availability in embryonic development and stem cell function. *Nat. Rev. Mol. Cell Biol.* **9**, 285–296 (2008).
4. J. D. Ochocki, M. C. Simon, Nutrient-sensing pathways and metabolic regulation in stem cells. *J. Cell Biol.* **203**, 23–33 (2013).
5. A. F. Baas, J. Kuipers, N. N. van der Wel, E. Batlle, H. K. Koerten, P. J. Peters, H. C. Clevers, Complete polarization of single intestinal epithelial cells upon activation of LKB1 by STRAD. *Cell* **116**, 457–466 (2004).
6. D. G. Hardie, D. R. Alessi, LKB1 and AMPK and the cancer-metabolism link - ten years after. *BMC Biol.* **11**, 36 (2013).
7. B. Y. Shorning, A. R. Clarke, Energy sensing and cancer: LKB1 function and lessons learnt from Peutz–Jeghers syndrome. *Semin. Cell Dev. Biol.* **52**, 21–29 (2016).
8. A. F. Baas, J. Boudeau, G. P. Sapkota, L. Smit, R. Medema, N. A. Morrice, D. R. Alessi, H. C. Clevers, Activation of the tumour suppressor kinase LKB1 by the STE20-like pseudokinase STRAD. *EMBO J.* **22**, 3062–3072 (2003).
9. D. B. Shackelford, Unravelling the connection between metabolism and tumorigenesis through studies of the liver kinase B1 tumour suppressor. *J. Carcinog.* **12**, 16 (2013).
10. S. P. Davies, A. T. R. Sim, D. G. Hardie, Location and function of three sites phosphorylated on rat acetyl-CoA carboxylase by the AMP-activated protein kinase. *Eur. J. Biochem.* **187**, 183–190 (1990).
11. G. F. Merrill, E. J. Kurth, D. G. Hardie, W. W. Winder, AICA riboside increases AMP-activated protein kinase, fatty acid oxidation, and glucose uptake in rat muscle. *Am. J. Physiol.* **273**, E1107–E1112 (1997).

12. D. M. Gwinn, D. B. Shackelford, D. F. Egan, M. M. Mihaylova, A. Mery, D. S. Vasquez, B. E. Turk, R. J. Shaw, AMPK phosphorylation of raptor mediates a metabolic checkpoint. *Mol. Cell* **30**, 214–226 (2008).
13. K. Inoki, T. Zhu, K.-L. Guan, TSC2 mediates cellular energy response to control cell growth and survival. *Cell* **115**, 577–590 (2003).
14. D. R. Alessi, K. Sakamoto, J. R. Bayascas, LKB1-dependent signaling pathways. *Annu. Rev. Biochem.* **75**, 137–163 (2006).
15. A. F. Hezel, N. Bardeesy, LKB1; linking cell structure and tumor suppression. *Oncogene* **27**, 6908–6919 (2008).
16. D. B. Shackelford, R. J. Shaw, The LKB1-AMPK pathway: Metabolism and growth control in tumour suppression. *Nat. Rev. Cancer* **9**, 563–575 (2009).
17. B. Y. Shorning, A. R. Clarke, LKB1 loss of function studied in vivo. *FEBS Lett.* **585**, 958–966 (2011).
18. S. E. Creuzet, J. P. Viallet, M. Ghawitian, S. Torch, J. Thélu, M. Alrajeh, A. G. Radu, D. Bouvard, F. Costagliola, M. Le Borgne, K. Buchet-Poyau, N. Aznar, S. Buschlen, H. Hosoya, C. Thibert, M. Billaud, LKB1 signaling in cephalic neural crest cells is essential for vertebrate head development. *Dev. Biol.* **418**, 283–296 (2016).
19. N. Bardeesy, M. Sinha, A. F. Hezel, S. Signoretti, N. A. Hathaway, N. E. Sharpless, M. Loda, D. R. Carrasco, R. A. DePinho, Loss of the Lkb1 tumour suppressor provokes intestinal polyposis but resistance to transformation. *Nature* **419**, 162–167 (2002).
20. V. Delmas, S. Martinozzi, Y. Bourgeois, M. Holzenberger, L. Larue, Cre-mediated recombination in the skin melanocyte lineage. *Genesis* **36**, 73–80 (2003).
21. I. Puig, I. Yajima, J. Bonaventure, V. Delmas, L. Larue, The tyrosinase promoter is active in a subset of vagal neural crest cells during early development in mice. *Pigment Cell Melanoma Res.* **22**, 331–334 (2009).
22. I. Yajima, S. Colombo, I. Puig, D. Champeval, M. Kumasaka, E. Belloir, J. Bonaventure, M. Mark, H. Yamamoto, M. M. Taketo, P. Choquet, H. C. Etchevers, F. Beermann, V. Delmas, L. Monassier, L. Larue, A subpopulation of smooth muscle cells, derived from melanocyte-competent precursors, prevents patent ductus arteriosus. *PLOS ONE* **8**, e53183 (2013).
23. P. Soriano, Generalized lacZ expression with the ROSA26 Cre reporter strain. *Nat. Genet.* **21**, 70–71 (1999).
24. I. Puig, D. Champeval, P. de Santa Barbara, F. Jaubert, S. Lyonnet, L. Larue, Deletion of Pten in the mouse enteric nervous system induces ganglioneuromatosis and mimics intestinal pseudoobstruction. *J. Clin. Invest.* **119**, 3586–3596 (2009).
25. B. Beirowski, E. Babetto, J. P. Golden, Y.-J. Chen, K. Yang, R. W. Gross, G. J. Patti, J. Milbrandt, Metabolic regulator LKB1 is crucial for Schwann cell-mediated axon maintenance. *Nat. Neurosci.* **17**, 1351–1361 (2014).
26. S. Pooya, X. Liu, V. B. S. Kumar, J. Anderson, F. Imai, W. Zhang, G. Ciraolo, N. Ratner, K. D. R. Setchell, Y. Yoshida, M. P. Jankowski, B. Dasgupta, The tumour suppressor LKB1 regulates myelination through mitochondrial metabolism. *Nat. Commun.* **5**, 4993 (2014).
27. Y.-A. A. Shen, Y. Chen, D. Q. Dao, S. R. Mayoral, L. Wu, D. Meijer, E. M. Ullian, J. R. Chan, Q. R. Lu, Phosphorylation of LKB1/Par-4 establishes Schwann cell polarity to initiate and control myelin extent. *Nat. Commun.* **5**, 4991 (2014).
28. S. Colombo, M. Kumasaka, C. Lobe, L. Larue, Genomic localization of the Z/EG transgene in the mouse genome. *Genesis* **48**, 96–100 (2010).
29. T. A. Heanue, V. Pachnis, Prospective identification and isolation of enteric nervous system progenitors using Sox2. *Stem Cells* **29**, 128–140 (2011).
30. D. L. Stemple, D. J. Anderson, Isolation of a stem cell for neurons and glia from the mammalian neural crest. *Cell* **71**, 973–985 (1992).
31. E. Dupin, L. Sommer, Neural crest progenitors and stem cells: From early development to adulthood. *Dev. Biol.* **366**, 83–95 (2012).
32. M. Bremer, F. Fröb, T. Kichko, P. Reeh, E. R. Tamm, U. Suter, M. Wegner, Sox10 is required for Schwann-cell homeostasis and myelin maintenance in the adult peripheral nerve. *Glia* **59**, 1022–1032 (2011).
33. K. R. Jessen, R. Mirsky, The origin and development of glial cells in peripheral nerves. *Nat. Rev. Neurosci.* **6**, 671–682 (2005).
34. J. Maurer, S. Fuchs, R. Jäger, B. Kurz, L. Sommer, H. Schorle, Establishment and controlled differentiation of neural crest stem cell lines using conditional transgenesis. *Differentiation* **75**, 580–591 (2007).
35. G. Beuster, K. Zarse, C. Kaleta, R. Thierbach, M. Kiehntopf, P. Steinberg, S. Schuster, M. Ristow, Inhibition of alanine aminotransferase in silico and in vivo promotes mitochondrial metabolism to impair malignant growth. *J. Biol. Chem.* **286**, 22323–22330 (2011).
36. D. B. Wang, C. Kinoshita, Y. Kinoshita, R. S. Morrison, p53 and mitochondrial function in neurons. *Biochim. Biophys. Acta* **1842**, 1186–1197 (2014).
37. S.-C. Lin, D. G. Hardie, AMPK: Sensing glucose as well as cellular energy status. *Cell Metab.* **27**, 299–313 (2018).
38. S. Gurumurthy, S. Z. Xie, B. Alagesan, J. Kim, R. Z. Yusuf, B. Saez, A. Tzatsos, F. Ozsolak, P. Milos, F. Ferrari, P. J. Park, O. S. Shirihai, D. T. Scadden, N. Bardeesy, The Lkb1 metabolic sensor maintains haematopoietic stem cell survival. *Nature* **468**, 659–663 (2010).
39. Y. Nakada, T. G. Stewart, C. G. Peña, S. Zhang, N. Zhao, N. Bardeesy, N. E. Sharpless, K. K. Wong, D. N. Hayes, D. H. Castrillon, The LKB1 tumor suppressor as a biomarker in mouse and human tissues. *PLOS ONE* **8**, e73449 (2013).
40. E. Q. Toyama, S. Herzig, J. Courchet, T. L. Lewis Jr., O. C. Losón, K. Hellberg, N. P. Young, H. Chen, F. Polleux, D. C. Chan, R. J. Shaw, AMP-activated protein kinase mediates mitochondrial fission in response to energy stress. *Science* **351**, 275–281 (2016).
41. R. Rattan, S. Giri, A. K. Singh, I. Singh, 5-Aminoimidazole-4-carboxamide-1-β-D-ribofuranoside inhibits cancer cell proliferation in vitro and in vivo via AMP-activated protein kinase. *J. Biol. Chem.* **280**, 39582–39593 (2005).
42. X. Liu, R. R. Chhipa, S. Pooya, M. Wortman, S. Yachyshin, L. M. L. Chow, A. Kumar, X. Zhou, Y. Sun, B. Quinn, C. McPherson, R. E. Warnick, A. Kendler, S. Giri, J. Poels, K. Norga, B. Viollet, G. A. Grabowski, B. Dasgupta, Discrete mechanisms of mTOR and cell cycle regulation by AMPK agonists independent of AMPK. *Proc. Natl. Acad. Sci. U.S.A.* **111**, E435–E444 (2014).
43. E. E. Vincent, P. P. Coelho, J. Blagih, T. Griss, B. Viollet, R. G. Jones, Differential effects of AMPK agonists on cell growth and metabolism. *Oncogene* **34**, 3627–3639 (2015).
44. Y. Zang, L.-F. Yu, T. Pang, L.-P. Fang, X. Feng, T.-Q. Wen, F.-J. Nan, L.-Y. Feng, J. Li, AICAR induces astroglial differentiation of neural stem cells via activating the JAK/STAT3 pathway independently of AMP-activated protein kinase. *J. Biol. Chem.* **283**, 6201–6208 (2008).
45. W. Liu, K. B. Monahan, A. D. Pfefferle, T. Shimamura, J. Sorrentino, K. T. Chan, D. W. Roadcap, D. W. Ollila, N. E. Thomas, D. H. Castrillon, C. R. Miller, C. M. Perou, K.-K. Wong, J. E. Bear, N. E. Sharpless, LKB1/STK11 inactivation leads to expansion of a prometastatic tumor subpopulation in melanoma. *Cancer Cell* **21**, 751–764 (2012).
46. T. Uesaka, S. Jain, S. Yonemura, Y. Uchiyama, J. Milbrandt, H. Enomoto, Conditional ablation of GFRα1 in postmigratory enteric neurons triggers unconventional neuronal death in the colon and causes a Hirschsprung's disease phenotype. *Development* **134**, 2171–2181 (2007).
47. T. Uesaka, M. Nagashimada, S. Yonemura, H. Enomoto, Diminished Ret expression compromises neuronal survival in the colon and causes intestinal aganglionosis in mice. *J. Clin. Invest.* **118**, 1890–1898 (2008).
48. S. A. Green, B. R. Uy, M. E. Bronner, Ancient evolutionary origin of vertebrate enteric neurons from trunk-derived neural crest. *Nature* **544**, 88–91 (2017).
49. T. Uesaka, M. Nagashimada, H. Enomoto, Neuronal differentiation in Schwann cell lineage underlies postnatal neurogenesis in the enteric nervous system. *J. Neurosci.* **35**, 9879–9888 (2015).
50. A. Furlan, I. Adameyko, Schwann cell precursor: A neural crest cell in disguise? *Dev. Biol.* **444**, S25–S35 (2018).
51. J. L. Coloff, J. P. Murphy, C. R. Braun, I. S. Harris, L. M. Shelton, K. Kami, S. P. Gygi, L. M. Selfors, J. S. Brugge, Differential glutamate metabolism in proliferating and quiescent mammary epithelial cells. *Cell Metab.* **23**, 867–880 (2016).
52. B. Smith, X. L. Schafer, A. Ambeskovic, C. M. Spencer, H. Land, J. Munger, Addiction to coupling of the Warburg effect with glutamine catabolism in cancer cells. *Cell Rep.* **17**, 821–836 (2016).
53. F. Kottakis, B. N. Nicolay, A. Roumane, R. Karnik, H. Gu, J. M. Nagle, M. Boukhali, M. C. Hayward, Y. Y. Li, T. Chen, M. Liesa, P. S. Hammerman, K. K. Wong, D. N. Hayes, O. S. Shirihai, N. J. Dyson, W. Haas, A. Meissner, N. Bardeesy, LKB1 loss links serine metabolism to DNA methylation and tumorigenesis. *Nature* **539**, 390–395 (2016).
54. X.-Y. Wang, S. Li, G. Wang, Z.-L. Ma, M. Chuai, L. Cao, X. Yang, High glucose environment inhibits cranial neural crest survival by activating excessive autophagy in the chick embryo. *Sci. Rep.* **5**, 18321 (2015).
55. X. Nie, J. Zheng, C. L. Ricupero, L. He, K. Jiao, J. J. Mao, mTOR acts as a pivotal signaling hub for neural crest cells during craniofacial development. *PLOS Genet.* **14**, e1007491 (2018).
56. C. Norrmén, G. Figlia, F. Lebrun-Julien, J. A. Pereira, M. Trötzmüller, H. C. Köfeler, V. Rantanen, C. Wessig, A.-L. F. van Deijk, A. B. Smit, M. H. G. Verheijen, M. A. Rüegg, M. N. Hall, U. Suter, mTORC1 controls PNS myelination along the mTORC1-RXRγ-SREBP-lipid biosynthesis axis in Schwann cells. *Cell Rep.* **9**, 646–660 (2014).
57. A. Preitschopf, K. Li, D. Schörghofer, K. Kinslechner, B. Schütz, H. Thi Thanh Pham, M. Rosner, G. J. Joo, C. Röhrl, T. Weichhart, H. Stangl, G. Lubec, M. Hengstschläger, M. Mikula, mTORC1 is essential for early steps during Schwann cell differentiation of amniotic fluid stem cells and regulates lipogenic gene expression. *PLOS ONE* **9**, e107004 (2014).
58. D. L. Sherman, M. Krols, L.-M. N. Wu, M. Grove, K.-A. Nave, Y. G. Gangloff, P. J. Brophy, Arrest of myelination and reduced axon growth when Schwann cells lack mTOR. *J. Neurosci.* **32**, 1817–1825 (2012).
59. B. Beirowski, K. M. Wong, E. Babetto, J. Milbrandt, mTORC1 promotes proliferation of immature Schwann cells and myelin growth of differentiated Schwann cells. *Proc. Natl. Acad. Sci. U.S.A.* **114**, E4261–E4270 (2017).
60. G. Figlia, C. Norrmén, J. A. Pereira, D. Gerber, U. Suter, Dual function of the PI3K-Akt-mTORC1 axis in myelination of the peripheral nervous system. *eLife* **6**, e29241 (2017).
61. C. Norrmén, G. Figlia, P. Pfistner, J. A. Pereira, S. Bachofner, U. Suter, mTORC1 is transiently reactivated in injured nerves to promote c-Jun elevation and Schwann cell dedifferentiation. *J. Neurosci.* **38**, 4811–4828 (2018).

62. A. J. Meijer, S. Lorin, E. F. Blommaart, P. Codogno, Regulation of autophagy by amino acids and MTOR-dependent signal transduction. *Amino Acids* **47**, 2037–2063 (2015).
63. L. Bar-Peled, D. M. Sabatini, Regulation of mTORC1 by amino acids. *Trends Cell Biol.* **24**, 400–406 (2014).
64. K. Hara, K. Yonezawa, Q.-P. Weng, M. T. Kozlowski, C. Belham, J. Avruch, Amino acid sufficiency and mTOR regulate p70 S6 kinase and eIF-4E BP1 through a common effector mechanism. *J. Biol. Chem.* **273**, 14484–14494 (1998).
65. J. Dyachok, S. Earnest, E. N. Iturraran, M. H. Cobb, E. M. Ross, Amino acids regulate mTORC1 by an obligate two-step mechanism. *J. Biol. Chem.* **291**, 22414–22426 (2016).
66. B. Daignan-Fornier, B. Pinson, 5-Aminoimidazole-4-carboxamide-1-beta-D-ribofuranosyl 5′-monophosphate (AICAR), a highly conserved purine intermediate with multiple effects. *Metabolites* **2**, 292–302 (2012).
67. E. Rao, Y. Zhang, Q. Li, J. Hao, N. K. Egilmez, J. Suttles, B. Li, AMPK-dependent and independent effects of AICAR and compound C on T-cell responses. *Oncotarget* **7**, 33783–33795 (2016).
68. B. Sid, C. Glorieux, M. Valenzuela, G. Rommelaere, M. Najimi, N. Dejeans, P. Renard, J. Verrax, P. B. Calderon, AICAR induces Nrf2 activation by an AMPK-independent mechanism in hepatocarcinoma cells. *Biochem. Pharmacol.* **91**, 168–180 (2014).
69. D. J. Asby, F. Cuda, M. Beyaert, F. D. Houghton, F. R. Cagampang, A. Tavassoli, AMPK activation via modulation of de novo purine biosynthesis with an inhibitor of ATIC homodimerization. *Chem. Biol.* **22**, 838–848 (2015).
70. A. Novak, C. Guo, W. Yang, A. Nagy, C. G. Lobe, Z/EG, a double reporter mouse line that expresses enhanced green fluorescent protein upon Cre-mediated excision. *Genesis* **28**, 147–155 (2000).
71. R. J. Shaw, N. Bardeesy, B. D. Manning, L. Lopez, M. Kosmatka, R. A. DePinho, L. C. Cantley, The LKB1 tumor suppressor negatively regulates mTOR signaling. *Cancer Cell* **6**, 91–99 (2004).
72. K. R. Laderoute, K. Amin, J. M. Calaoagan, M. Knapp, T. Le, J. Orduna, M. Foretz, B. Viollet, 5′-AMP-activated protein kinase (AMPK) is induced by low-oxygen and glucose deprivation conditions found in solid-tumor microenvironments. *Mol. Cell. Biol.* **26**, 5336–5347 (2006).
73. N. Tricaud, C. Perrin-Tricaud, J. L. Brusés, U. Rutishauser, Adherens junctions in myelinating Schwann cells stabilize Schmidt-Lanterman incisures via recruitment of p120 catenin to E-cadherin. *J. Neurosci.* **25**, 3259–3269 (2005).
74. V. Govindaraju, K. Young, A. A. Maudsley, Proton NMR chemical shifts and coupling constants for brain metabolites. *NMR Biomed.* **13**, 129–153 (2000).
75. F. Fauvelle, P. Carpentier, F. Dorandeu, A. Foquin, G. Testylier, Prediction of neuroprotective treatment efficiency using a HRMAS NMR-based statistical model of refractory status epilepticus on mouse: A metabolomic approach supported by histology. *J. Proteome Res.* **11**, 3782–3795 (2012).
76. O. Behar, H. Ovadia, R. D. Polakiewicz, H. Rosen, Lipopolysaccharide induces proenkephalin gene expression in rat lymph nodes and adrenal glands. *Endocrinology* **134**, 475–481 (1994).
77. D. Zietkowski, R. L. Davidson, T. R. Eykyn, S. S. de Silva, N. M. Desouza, G. S. Payne, Detection of cancer in cervical tissue biopsies using mobile lipid resonances measured with diffusion-weighted ^{1}H magnetic resonance spectroscopy. *NMR Biomed.* **23**, 382–390 (2010).
78. N. Bondurand, D. Natarajan, A. Barlow, N. Thapar, V. Pachnis, Maintenance of mammalian enteric nervous system progenitors by SOX10 and endothelin 3 signalling. *Development* **133**, 2075–2086 (2006).
79. A. Chalazonitis, A. A. Tang, Y. Shang, T. D. Pham, I. Hsieh, W. Setlik, M. D. Gershon, E. J. Huang, Homeodomain interacting protein kinase 2 regulates postnatal development of enteric dopaminergic neurons and glia via BMP signaling. *J. Neurosci.* **31**, 13746–13757 (2011).
80. H. Enomoto, T. Araki, A. Jackman, R. O. Heuckeroth, W. D. Snider, E. M. Johnson Jr., J. Milbrandt, GFRα1-deficient mice have deficits in the enteric nervous system and kidneys. *Neuron* **21**, 317–324 (1998).
81. P. Nony, H. Gaude, M. Rossel, L. Fournier, J.-P. Rouault, M. Billaud, Stability of the Peutz-Jeghers syndrome kinase LKB1 requires its binding to the molecular chaperones Hsp90/Cdc37. *Oncogene* **22**, 9165–9175 (2003).

Acknowledgments: We are grateful to E. Fontaine and K. Padmanabhan for helpful comments about the results. We thank J. Courchet, B. Viollet, and J. Maurer for sharing cells and reagents. We thank S. Michallet, B. Sefrin, and P. Vernet from the animal facility of the Institute for Advanced Biosciences and F. Blanquet and C. Colomb from the animal facility PHTA of Grenoble. We are grateful to D. Bouvard for giving us the R26R mice and to G. Chevallier for help with mouse breeding and genotyping. We thank V. Blanc-Marquis for technical help. S. Michallet and M. Schweitzer were very helpful with excellent technical assistance. C. Caron helped us with human sample studies. This work benefited from the help of T. Dufourd and M. Aguilera during their internships in the laboratory. J. Delaroche and A. Bertrand from the electron microscopy facility of the Neuroscience Institute of Grenoble performed semithin sections, staining, and electronic microscopy experiments and analyses. We thank N. Gadot and the ANIPATH facility, University Lyon1 Laennec, for tissue sections. **Funding:** This work was founded by "l'Institut National du Cancer" (Programme recherche translationnelle en cancérologie), "la Ligue régionale contre le cancer" (comité de l'Isère R17030CC), "l'Association pour la Recherche sur le Cancer" (Fondation ARC R17158CC), and NIH/NCI (1R01CA219670-01A1).
Author contributions: A.G.R., S.T., C.T., and M.B. conceived the project, designed the studies, and analyzed and interpreted the data. V.D. and L.Lar. generated the Tyr::Cre mouse model. S.T. and M.B. generated the Tyr::Cre Lkb1 cKO mouse model. A.G.R., S.T., C.T., A.L., and V.D. performed histological analyses for phenotypic characterization. A.G.R., S.T., C.T., and M.B. conducted and analyzed all in cellulo experiments. C.T. and F.F. performed, analyzed, and quantified HRMAS NMR experiments. S.T. and K.P.-G. performed the electron microscopy experiments and quantifications. A.G.R., R.B., and C.T. conducted and analyzed the reverse transcription quantitative PCR (RT-qPCR). V.P. and N.Bo. advised on enteric nervous system analyses. N.T. advised on Schwann cell analyses. U.S. assisted in metabolic analyses and interpretations. L.Laf., P.H., and L.Lar. advised us throughout the study. S.T., C.T., M.B., L.Lar., and N.Ba. wrote the manuscript. A.G.R., V.P., N.Bo., N.T., L.Laf., U.S., and P.H. commented on the manuscript. **Competing interests:** The authors declare that they have no competing interests. **Data and materials availability:** All data needed to evaluate the conclusions in the paper are present in the paper and/or the Supplementary Materials. Additional data related to this paper may be requested from the authors.

Submitted 25 June 2018
Accepted 10 June 2019
Published 17 July 2019
10.1126/sciadv.aau5106

Citation: A. G. Radu, S. Torch, F. Fauvelle, K. Pernet-Gallay, A. Lucas, R. Blervaque, V. Delmas, U. Schlattner, L. Lafanechère, P. Hainaut, N. Tricaud, V. Pingault, N. Bondurand, N. Bardeesy, L. Larue, C. Thibert, M. Billaud, LKB1 specifies neural crest cell fates through pyruvate-alanine cycling. *Sci. Adv.* **5**, eaau5106 (2019).

LKB1 specifies neural crest cell fates through pyruvate-alanine cycling

Anca G. Radu, Sakina Torch, Florence Fauvelle, Karin Pernet-Gallay, Anthony Lucas, Renaud Blervaque, Véronique Delmas, Uwe Schlattner, Laurence Lafanechère, Pierre Hainaut, Nicolas Tricaud, Véronique Pingault, Nadège Bondurand, Nabeel Bardeesy, Lionel Larue, Chantal Thibert and Marc Billaud

Sci Adv **5** (7), eaau5106.
DOI: 10.1126/sciadv.aau5106